ARTICLES
https://doi.org/10.1038/s41556-018-0220-2
nature cell biology

Reticular adhesions are a distinct class of cell-matrix adhesions that mediate attachment during mitosis

John G. Lock[1,2,7*], Matthew C. Jones[3,7], Janet A. Askari[3], Xiaowei Gong[2], Anna Oddone[4,5], Helene Olofsson[2], Sara Göransson[2], Melike Lakadamyali[5,6], Martin J. Humphries[3] and Staffan Strömblad[2*]

Adhesion to the extracellular matrix persists during mitosis in most cell types. However, while classical adhesion complexes, such as focal adhesions, do and must disassemble to enable mitotic rounding, the mechanisms of residual mitotic cell–extracellular matrix adhesion remain undefined. Here, we identify 'reticular adhesions', a class of adhesion complex that is mediated by integrin αvβ5, formed during interphase, and preserved at cell–extracellular matrix attachment sites throughout cell division. Consistent with this role, integrin β5 depletion perturbs mitosis and disrupts spatial memory transmission between cell generations. Reticular adhesions are morphologically and dynamically distinct from classical focal adhesions. Mass spectrometry defines their unique composition, enriched in phosphatidylinositol-4,5-bisphosphate (PtdIns(4,5)P_2)-binding proteins but lacking virtually all consensus adhesome components. Indeed, reticular adhesions are promoted by PtdIns(4,5)P_2, and form independently of talin and F-actin. The distinct characteristics of reticular adhesions provide a solution to the problem of maintaining cell–extracellular matrix attachment during mitotic rounding and division.

Cell–extracellular matrix (ECM) attachment occurs through a range of integrin-containing adhesion complexes, including focal complexes, focal adhesions and fibrillar adhesions[1,2], and modulates many processes including cell movement, proliferation and differentiation[3]. Although structurally and functionally varied, adhesion complexes overlap substantially in their composition, sharing a 60-protein consensus adhesome[4]. As one of the most abundant consensus adhesome proteins, talin-1 is viewed as an indispensable contributor to integrin activation[5] and adhesion complex organization[6]. Adaptor proteins that couple integrins to F-actin, such as vinculin and paxillin, are also universally associated with adhesion complexes, reflecting the pivotal role of F-actin in adhesion complex function[7].

Cell–ECM adhesion is also critical for mitotic progression and for the transmission of spatial memory between generations[8–11], a key factor controlling differentiation and tissue development[12]. Paradoxically, the importance of cell–ECM attachment during mitosis conflicts with the observed disassembly of classical adhesion complexes at mitotic onset[13], because failure of adhesion complex disassembly perturbs division[14,15]. Furthermore, integrins implicated in mitotic adhesion, such as β1, function not at the adhesion plane but in the detached cell cortex[16]. Overall, the nature of mitotic adhesion complexes remains profoundly unclear[17,18].

Here, we identify a class of 'reticular' adhesion complex with a unique adhesome, formed by integrin αVβ5 during interphase in the absence of both talin and F-actin. Reticular adhesions persist throughout mitosis, providing the ECM anchoring that is necessary for efficient division. Thus, reticular adhesions provide a solution to the paradox of mitotic cell–ECM attachment.

Results

αVβ5 is the predominant integrin used by cells in long-term culture. The integrin consensus adhesome was derived from cells plated on fibronectin[4,19]. To study the adhesome of cells that had assembled their own ECM, we performed mass spectrometry (MS) analysis of adhesion complex composition in U2OS cells following 72 h of growth. Unexpectedly, the most abundant integrin subunits identified were αV and β5, with much lower levels of β1, β3, β8, α5 and α3 (Fig. 1a). Subsequent immunofluorescence analysis confirmed that very distinct αVβ5-positive adhesion complexes were visible in a range of cells in long-term culture, with little αVβ3 or β1 labelling detected in U2OS, A549 and A375 cells (Fig. 1b and Supplementary Fig. 1a). Notably, αVβ5 was simultaneously detected in classical focal adhesions at the cell periphery and in reticular structures across the cell body, also visible after 24 and 48 h of cell growth (Supplementary Fig. 1b). U2OS cells were then plated on the integrin αV ligand vitronectin. Confocal imaging showed β5 associated with two different structures following 3 h of spreading: peripheral focal adhesion complexes containing talin and vinculin, and centrally distributed, punctate or reticular structures lacking these components (Fig. 1c,d).

Subsequently, similar αVβ5-positive, talin-negative structures were detected in each of nine cell lines assessed, including the cancer cell lines CS1-b5, HeLa, MCF7 and BT549 (Supplementary

[1]Department of Pathology, School of Medical Sciences, University of New South Wales, Sydney, Australia. [2]Department of Biosciences and Nutrition, Karolinska Institutet, Huddinge, Sweden. [3]Wellcome Trust Centre for Cell-Matrix Research, Faculty of Biology, Medicine and Health, University of Manchester, Manchester, UK. [4]Centre for Genomic Regulation (CRG), The Barcelona Institute of Science and Technology, Barcelona, Spain. [5]ICFO, Institut de Ciencies Fotoniques, Mediterranean Technology Park, The Barcelona Institute of Science and Technology, Castelldefels, Barcelona, Spain. [6]Perelman School of Medicine, Department of Physiology, University of Pennsylvania, Philadelphia, PA, USA. [7]These authors contributed equally: John G. Lock, Matthew C. Jones. *e-mail: john.lock@unsw.edu.au; staffan.stromblad@ki.se

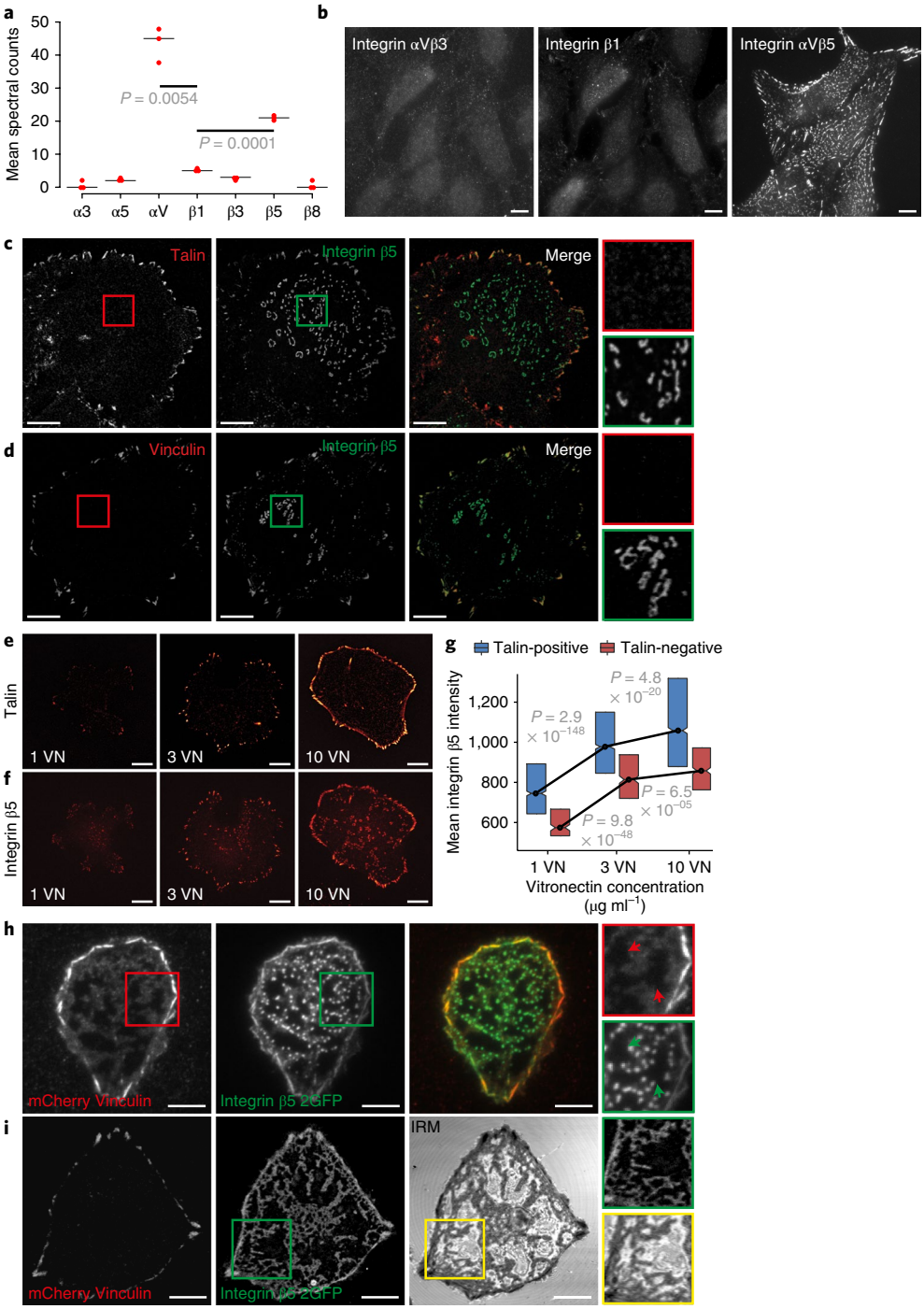

Fig. 1 | Integrin αVβ5 forms novel talin- and vinculin-negative reticular adhesion structures. a, MS analysis of integrin subunits detected in adhesions isolated (after cell removal) from U2OS cells grown in complete medium for 3 days on tissue culture plastic. Results are mean spectral counts from $n = 3$ biologically independent experiments, where thin horizontal lines indicate median values. *P* values reflect comparison via two-sided unpaired *t*-testing between integrin subunits αv or β5 and the next highest expressed subunit, β1. **b**, Confocal images of immuno-fluorescently labelled integrins αVβ3 (LM609), β1 (9EG7) and αVβ5 (15F11) for U2OS cells plated on glass coverslips for 72 h. **c**–**f**, U2OS cells were plated for 3 h in serum-free medium on surfaces coated with 10 μg ml^{-1} vitronectin (VN), except where specified otherwise. **c**,**d**, Confocal images of talin (**c**) or vinculin (**d**) immunofluorescence with that of integrin β5. Boxed areas are shown at higher magnification to the right. **e**,**f**, Co-labelling of talin (**e**) and β5 (**f**) in cells grown on glass coated with 1, 3 or 10 μg ml^{-1} VN. **g**, Quantified intensities of talin-positive (blue) or -negative (red) β5 structures. Data are taken from 81 cells (>23 per condition) and $n = 6{,}132$ adhesions derived from three biologically independent experiments. Boxplot centre and box edges indicate median and 25th or 75th percentiles, respectively. Boxplot notches approximate 95% CIs (see Methods for details). *P* values reflect two-sided unpaired Mann–Whitney *U*-testing. **h**, TIRF images of an mCherry-vinculin- and β5-2GFP-expressing U2OS cell (U2OS-β5V). Arrows in magnified boxes highlight regions lacking vinculin signal, which fall between β5-positive, vinculin-negative puncta. **i**, Confocal and interference reflection microscopy (IRM) images of a U2OS-β5V cell exemplify correlations between β5-positive, vinculin-negative structures and regions with close cell–substrate proximity. All images are representative of results from at least three biologically independent experiments. Scale bars, 10 μm. Source data for **a** and **g** are available in Supplementary Table 1.

Fig. 1c), immortalized non-transformed HME1 and RPE1 cells (Supplementary Fig. 1d), and primary mouse aortic endothelial (MAE) and human dermal fibroblast (HDF) cells (Supplementary Fig. 1e), indicating that formation of αVβ5-positive, talin-negative structures is characteristic of a wide range of cell types. Integrin αV and β5 subunits co-localized (Supplementary Fig. 2a), but co-labelling of β5 with antibodies against various adhesion complex-related proteins, including consensus adhesome components, αVβ5 binding partners, cytoskeletal proteins (including F-actin) and phosphotyrosine, revealed no specific co-localization (Supplementary Figs. 1c and 2b–m). Integrin β5 labelling intensity in both talin-1-positive and -negative structures correlated with vitronectin concentrations (Fig. 1E-G), while U2OS cells plated on laminin (not a ligand for αVβ5) only formed vinculin-positive adhesion complexes (Supplementary Fig. 2n). In conclusion, formation of the reticular structures depends on αVβ5–ECM ligand binding.

We next labelled the integrin β5 extracellular domain without prior cell permeabilization (Supplementary Fig. 2o). Strong co-localisation with integrin β5-2GFP demonstrated αVβ5 plasma membrane embedding and antibody specificity. Moreover, total internal reflection (TIRF) imaging of live U2OS cells co-expressing β5-2GFP and mCherry-vinculin (U2OS-β5V) revealed central, αVβ5-positive, vinculin-negative structures in the TIRF plane (Fig. 1h). Dark intracellular regions in mCherry-vinculin signals indicated where tensioned ventral membranes arced out of the TIRF plane, leaving no cytoplasmic signal. These dark regions corresponded to large gaps between αVβ5-positive, vinculin-negative puncta, suggesting the latter to be attachment points that pin the ventral plasma membrane to the substrate. This hypothesis was supported by live cell interference reflection microscopy, where close cell–substrate proximity corresponded precisely with integrin β5-2GFP signals in both vinculin-positive FAs and vinculin-negative structures (Fig. 1i). Collectively, these data indicate that αVβ5-positive, consensus adhesome component-negative reticular structures are bona fide cell–ECM adhesion complexes. These are hereafter termed 'reticular adhesions'.

Reticular and focal adhesion complexes are morphologically and dynamically distinct. Reticular adhesions were more numerous than classical focal adhesion complexes at all sizes (Fig. 2a), increased in size more frequently (Fig. 2b) and were localized further from the cell periphery (Fig. 2c). There was no correlation between RA size and integrin β5 clustering density, unlike the increased integrin density observed in larger FAs (Fig. 2d)[20,21]. This implies molecular-scale differences between the maturation of focal and reticular adhesions, with the latter being more homogenous. Reticular adhesions formed as small puncta, grew by net peripheral integrin recruitment, producing ring-like or reticular structures that ultimately fragmented and disassembled, all without recruiting vinculin (Fig. 2e–h, Supplementary Movie 1 and cropped region from Fig. 2h in Supplementary Movie 2). Thus, reticular adhesions form de novo as a distinct class of adhesion complex.

Quantitative tracking highlighted stark differences in dynamics between reticular adhesions and focal adhesions (Fig. 2i–n and Supplementary Movie 3): isotropic reticular adhesion growth produced low displacement (Fig. 2j), whereas focal adhesions elongated anisotropically and slid at high velocities, reflecting F-actin-derived forces driving asymmetric component recruitment (Fig. 2k)[22,23]. Isotropic growth and immobility in reticular adhesions suggests the absence of such directed mechanical cues[24] and complements the observed lack of F-actin. This conclusion was supported by locally disordered motion of reticular adhesion trajectories (Fig. 2l). In contrast, focal adhesions moved co-linearly within different cell lobes (Fig. 2m), reflecting aligned, centripetal F-actin-derived forces[25]. The relationship between average adhesion complex velocity and lifetime revealed that, for both focal adhesions and reticular adhesions, fast movement corresponded to short lifetime. Thus, fast-moving focal adhesions existed for less than half the lifespan of reticular adhesions, which were relatively static and long-lived (Fig. 2n).

Fluorescence recovery after photobleaching analysis revealed that, despite their increased lifetime as complexes, β5-2GFP turnover in reticular adhesions was faster and more extensive than in focal adhesions (Fig. 3a–e and Supplementary Movie 4). Conversely, variability in β5-2GFP fluorescence recovery was lower in reticular adhesions (Fig. 3f), suggesting relative homogeneity in molecular organization and dynamics across their lifespan, consistent with the homogeneity in integrin clustering densities (Fig. 2d).

In stochastic optical reconstruction microscopy (STORM), both adhesion complex types displayed small internal clusters of integrin β5 (Fig. 3g), consistent with the integrin β1 nanocluster organization within adhesion complexes that we recently reported[26]. Minimal differences were observed between the adhesion complex types in terms of nearest-neighbour distances between nanoclusters and molecular localization counts per nanocluster (Fig. 3h,i). Thus, despite the absence of consensus adhesome components (including talin-1, thought to control nanoscale integrin organization[6]) and differences in macromolecular dynamics, the molecular-scale organization of integrin β5 is virtually identical in focal adhesions and reticular adhesions.

Reticular adhesions mediate cell attachment but form independently of F-actin and talin. Disruption of actin polymerization by cytochalasin D or latrunculin A before cell–ECM attachment inhibited focal adhesion, but not reticular adhesion, formation (Fig. 4a,b, Supplementary Fig. 3a and Supplementary Movie 5; note the simultaneous formation of both reticular adhesions and focal adhesions within 20–30 min of control cell attachment). Cytochalasin D inhibited cell spreading, but not reticular adhesion numbers relative to cell area, as evidenced by matched linear trends in cell area versus adhesion complex number within treated and control cells (Fig. 4c). Notably, while cytochalasin D substantially reduced vinculin levels in surviving focal adhesions, β5 density increased in reticular adhesions (Fig. 4d). Furthermore, cytochalasin D treatment after attachment caused disassembly of focal adhesions, but retention of reticular adhesions (Supplementary Fig. 3a).

Integrin β3- and β5-negative CS1-wt cells did not attach to vitronectin, while CS1 cells stably expressing β5 (CS1-β5) attached strongly (Fig. 4e and Supplementary Fig. 3b) and formed both focal and reticular adhesions. CS1-β5 cells treated with cytochalasin D attached approximately half as strongly as unperturbed CS1-β5 cells, demonstrating that reticular adhesions facilitate cell attachment in the absence of F-actin. This residual adhesion was blocked by competitive inhibition of αVβ5-VN (vitronectin) binding using cyclic RGD (Arg-Gly-Asp) peptides, confirming αVβ5 specificity (Fig. 4e). Thus, reticular adhesions forming in the absence of F-actin facilitate attachment in the absence of focal adhesions.

To assess the role of talin in reticular adhesion formation, talin-1-null mouse embryonic stem cells (mES talin-1$^{-/-}$) were transfected with talin-2 siRNA. Reduction of talin limited cell spreading (Fig. 4f–h and Supplementary Fig. 3c)[27] and ablated focal adhesions (Fig. 4f,g); however, integrin β5 was more densely concentrated within reticular adhesions following talin-2 knockdown (Fig. 4f,g,i), similar to cells treated with cytochalasin D (Fig. 4a–d). Thus, reticular adhesions can form independently of talin. On activation by manganese or the talin-1 head domain, integrin αVβ3 forms reticular-like clusters in the centre of the cell[28,29]. In contrast, αVβ5 clustered independently of talin or additional activation stimuli. Furthermore, mRFP-tagged talin-1 head or rod domains neither localized to reticular adhesions nor altered αVβ5-containing

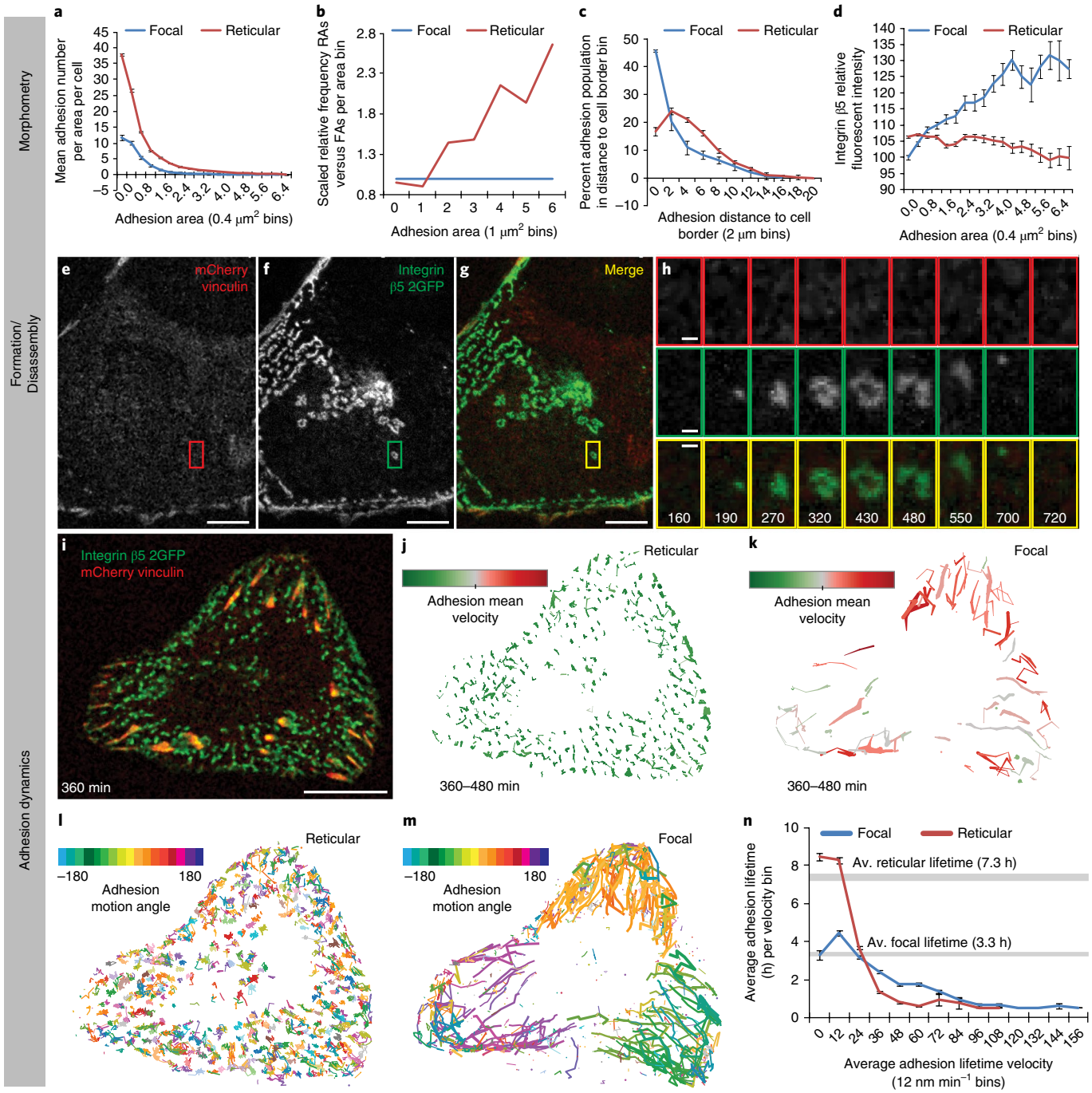

Fig. 2 | Comparison of focal and reticular adhesion morphometry and dynamics. a, Histogram of focal (blue) and reticular (red) adhesions by area (error bars represent 95% CI). **b**, Frequency of reticular adhesions by area, represented as fold-change relative to focal adhesions. **c**, Percentage of adhesions versus distance from cell border (error bars represent 95% CI). **d**, Adhesion area versus mean integrin β5 intensity relative to smallest focal adhesions (error bars represent 95% CI). **e**–**g**, Representative images from live imaging of mCherry-vinculin (**e**) and β5-2GFP (**f**) (merged in **g**; Supplementary Movie 1). **h**, Zoomed regions of **e**–**g** at the time points indicated (mins) (Supplementary Movie 2). Scale bars, 10 μm (**e**–**g**) and 1 μm (**h**). (**i**–**m** derived from Supplementary Movie 3). **i**, Merged image of β5-2GFP and mCherry-vinculin at a representative time point. **j**,**k**, Trajectories of reticular (**j**) and focal (**k**) adhesions colour-coded by mean velocity (green, slow; red, fast). **l**,**m**, Trajectories of reticular (**l**) and focal (**m**) adhesions colour-coded by net adhesion motion angle. Line thicknesses indicate instantaneous adhesion velocity. **n**, Aggregate analysis of all trajectories of average adhesion velocity versus corresponding average adhesion lifetime (dashed lines indicate adhesion class average lifetimes; error bars represent 95% CI). Data in **a**–**n** derive from live imaging and analysis of 14 U2OS-β5V cells (in four biologically independent experiments) over 12 h (10 min intervals), providing $n = 30{,}123$ focal adhesion and $n = 91{,}898$ reticular adhesion observations. Source data for **a**–**d** and **n** are available in Supplementary Table 1.

reticular adhesions (Supplementary Fig. 3d). Expression of enhanced green fluorescent protein (EGFP)-tagged integrin β5 extracellular domain fused to the integrin β3 tail domain also demonstrated localization to reticular adhesions (Fig. 4j,k), identifying the β5 extracellular domain as the key facilitator of αVβ5 clustering in reticular adhesions.

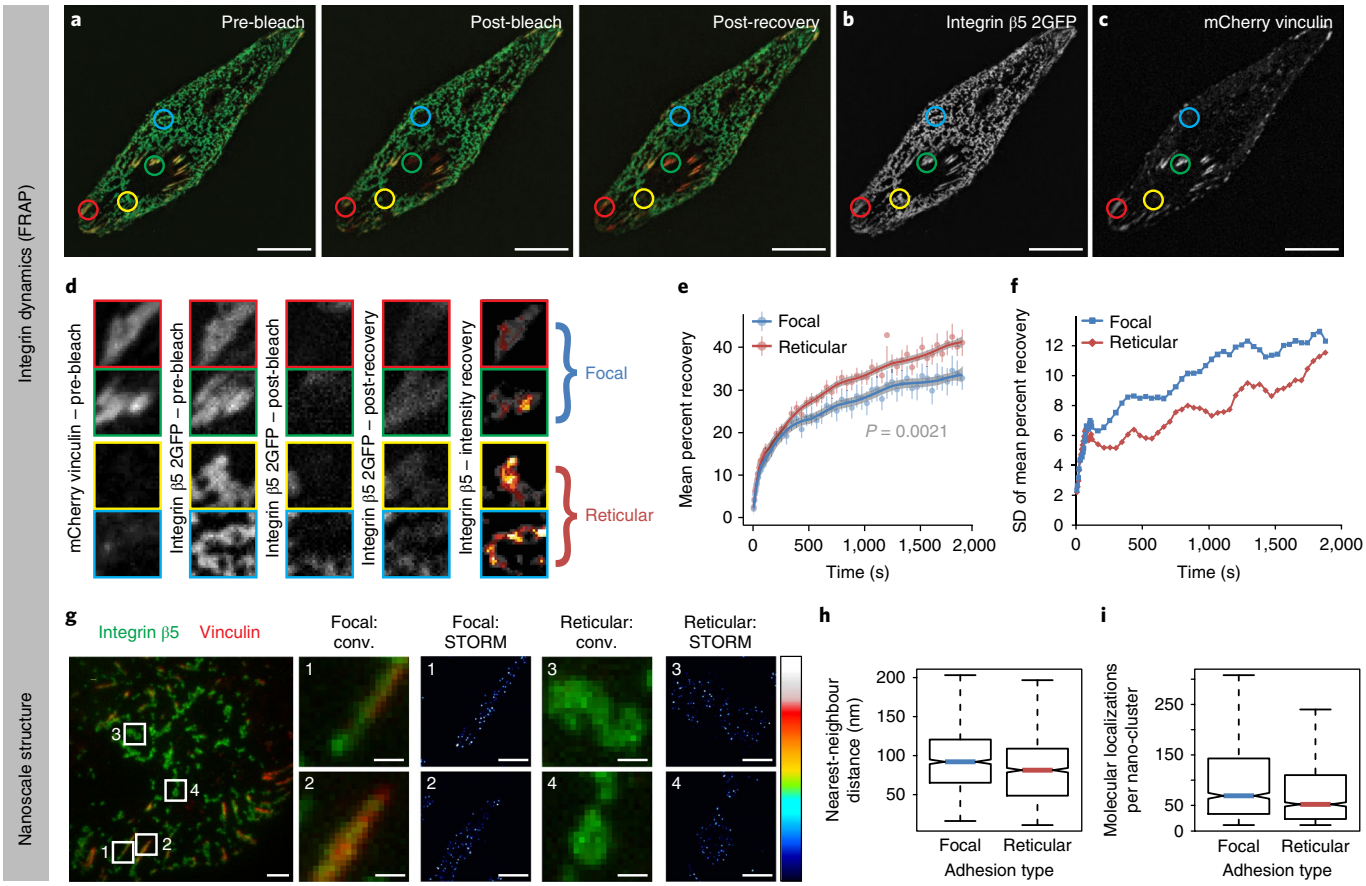

Fig. 3 | Comparison of focal and reticular adhesion integrin dynamics and nanoscale structure. a, Integrin β5-2GFP and mCherry-vinculin pre-bleach, post-bleach and post-recovery (30 min; Supplementary Movie 4). **b**,**c**, Circles indicate focal and reticular adhesion bleach regions, supported by single channel images. Scale bars, 10 µm (**a**–**c**). **d**, Square regions corresponding to circles in **a**–**c**. Fifth column: colour-scaled images (low to high values: black, red, orange, yellow, white) of intensity recovery for focal and reticular adhesions. **e**, Aggregate FRAP recovery curves for $n = 63$ focal and $n = 68$ reticular adhesions (from 15 cells across three biologically independent experiments). Recovery curves are displayed as mean per time point (circles) ± 95% CI. Loess regression defines a smoothed fit (lines) ± a moving 95% CI envelope. *P* values reflect comparison of Loess fitted curves assessed via two-sided unpaired Kolmogorov–Smirnov testing. **f**, Post-bleach recovery time versus standard deviation of recovery at each time point. **g**–**i**, Comparison of integrin β5 nanoclustering. **g**, β5 immuno-labelling and mCherry-vinculin in a U2OS cell plated on VN and imaged via confocal microscopy. Representative focal (1 and 2) and reticular adhesions (3 and 4) cropped from matched confocal and STORM images (β5 only, 'royal' look-up table intensity-scaled as in legend). Scale bars, 2 µm (500 nm in cropped images). **h**,**i**, β5 nanocluster nearest-neighbour distances (**h**) and molecular localization counts per nanocluster (**i**) based on STORM data. 216 focal and 162 reticular adhesions were assessed, including $n = 5{,}530$ nanoclusters across four biologically independent experiments. Boxplot centre and box edges indicate median and 25th or 75th percentiles, respectively, while whiskers indicate the median ± 1.5 × IQR (interquartile range) or the most extreme observations within these limits. Boxplot notches approximate 95% CIs. Source data for **e**, **f** and **h**, **i** are provided in Supplementary Table 1.

Reticular adhesion composition is unique. We next used MS to define reticular adhesion composition. U2OS cells were treated with cytochalasin D to deplete focal adhesions, followed by ventral membrane adhesion complex isolation and processing. A total of 199 proteins were identified in the control condition, 18 of which were consensus adhesome components (Fig. 5a and Supplementary Table 2)[4]. Conversely, cytochalasin D-treated samples revealed 53 proteins selectively associated with reticular adhesions, only one of which was a consensus adhesome protein (tensin-3). Four proteins were discounted from further analysis due to exceptionally high representation in the CRAPome database[30], leaving a reticular adhesome of 49 proteins. Of these, 41 formed a highly connected protein–protein interaction network (Fig. 5b). Lower diversity in the reticular adhesome supports evidence of relative homogeneity in both integrin clustering density (Fig. 2d) and dynamics (Fig. 3f). Gene ontology analysis revealed enrichment of terms relating to membrane organization and endocytosis (Fig. 5c,d), in contrast to the control condition that was enriched for terms related to cell adhesion and regulation of actin cytoskeleton (Supplementary Fig. 4a,b). Ontology analysis was consistent with MS identification of a number of known endocytic adaptors in reticular adhesions (Fig. 5b). Six candidates were validated by immunofluorescence, including NUMB, DAB2 (Fig. 5e,f), EPS15L1, HIP1R, WASL and ITSN1 (Supplementary Fig. 4c–f). Despite the observation that reticular adhesions did not associate with F-actin and formed following disruption of F-actin, a number of actin-binding proteins were identified in the reticular adhesome and two of these (tensin-3 and talin-2) co-localized with β5 in cytochalasin-treated cells (Fig. 5g,h). In contrast, the Arp2/3 complex component Arp3 did not localize with β5-positive structures (Supplementary Fig. 4g) and inhibition of Arp2/3 did not abrogate reticular adhesions, despite reducing focal adhesion intensity (Supplementary Fig. 5a–c).

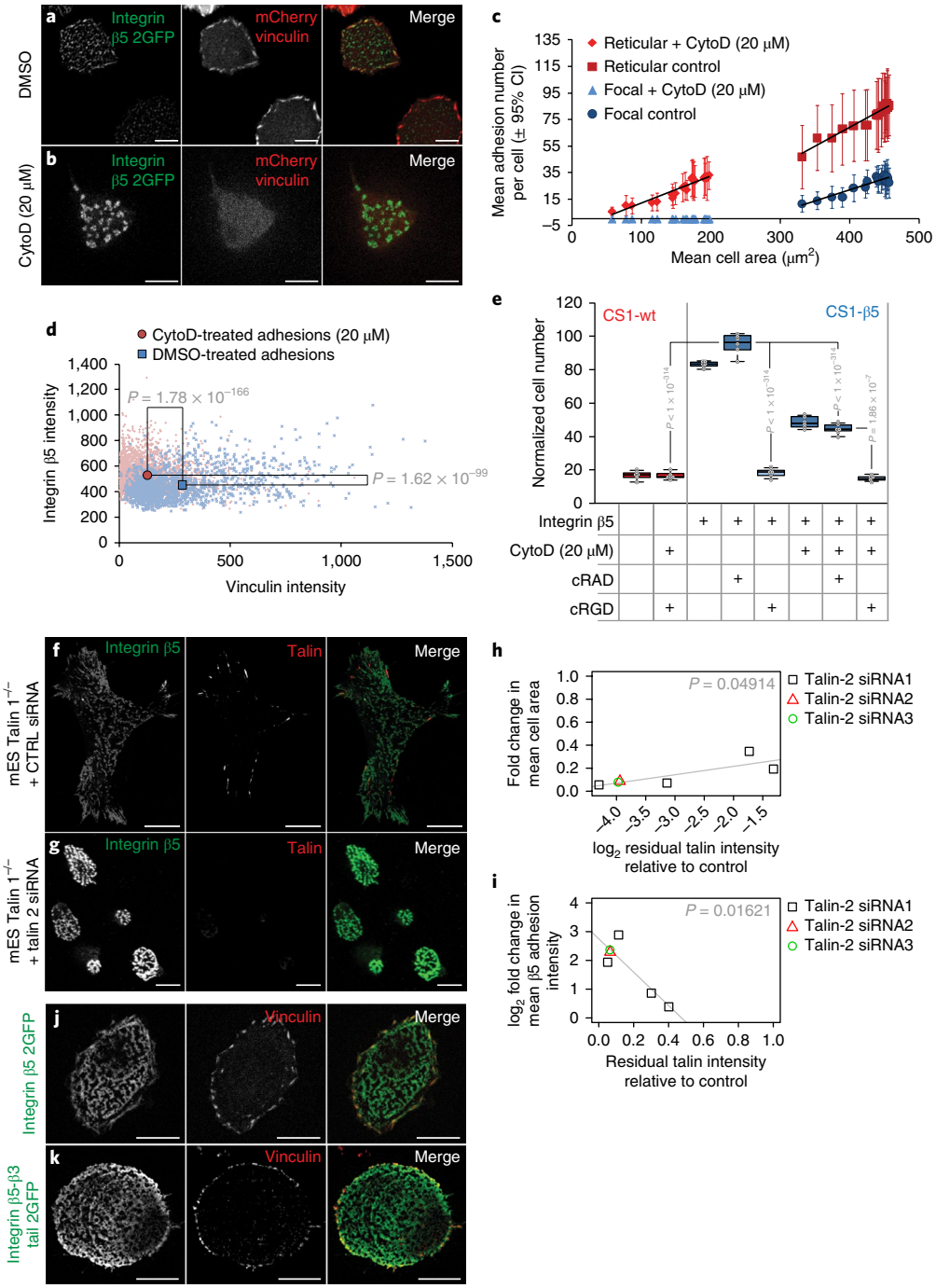

Fig. 4 | Reticular adhesions form in the absence of F-actin and talin. a,**b**, Confocal images of integrin β5-2GFP and mCherry-vinculin in cells pre-treated in suspension and during spreading on VN with DMSO (**a**) or 20 μM cytochalasin D (CytoD) (**b**) (Supplementary Movie 5). **c**, Cell area versus reticular (red) or focal (blue) adhesion number following the indicated treatments (means ± /95% CI; black lines, linear regression, 12 cells per condition, $n = 7{,}018$ focal and $n = 4{,}570$ reticular adhesions across three biologically independent experiments). **d**, Quantification of immuno-labelling intensities for vinculin and β5 per adhesion in U2OS cells attached to VN and treated with DMSO (blue) or CytoD (red). CytoD significantly reduces vinculin intensities but increases β5 (*P* values reflect two-sided unpaired Mann–Whitney *U*-testing, 2,533 adhesions from 22 DMSO-treated cells; 1,410 adhesions from 18 CytoD-treated cells across $n = 3$ biologically independent experiments). **e**, Boxplots summarizing $n = 6$ biologically independent attachment assays using CS1-wt (lacking αVβ5) and CS1-β5 (expressing αVβ5) cells in the presence or absence of 20 μM CytoD and/or non-inhibitory cyclic RAD peptides and/or αVβ5 inhibitory cyclic RGD peptides. Cell attachment relative to maximum (=100) CS1-β5 + cRAD. Boxplot centre and box edges indicate median and quartiles while whiskers indicate median ± 1.5 × IQR or the most extreme observations within these limits. *P* values reflect two-sided unpaired *t*-testing with Holm–Bonferroni correction for multiple tests. **f**,**g**, Representative confocal images of mES talin-1$^{-/-}$ cells transfected with control (**f**) or talin-2-specific siRNAs (**g**) plated on VN and immuno-labelled against β5 and talin-2. **h**,**i**, Single cell (as in **f** and **g**) based quantification of residual talin expression versus cell spread area (**h**) or mean β5 intensity (**i**) in segmented adhesions standardized as fold-change relative to each internal control, summarized across $n = 6$ independent experiments. Linear regression *P* values: correspondence between residual talin levels and cell area or β5 adhesion intensity. **j**,**k**, Confocal images (representative of three biologically independent experiments) of U2OS cells expressing integrin β5-2GFP or integrin β5-β3-tail-2GFP plated on VN and immuno-labeled against vinculin. Scale bars, 10 μm. Source data for **c**–**e** and **h**, **i** are provided in Supplementary Table 1.

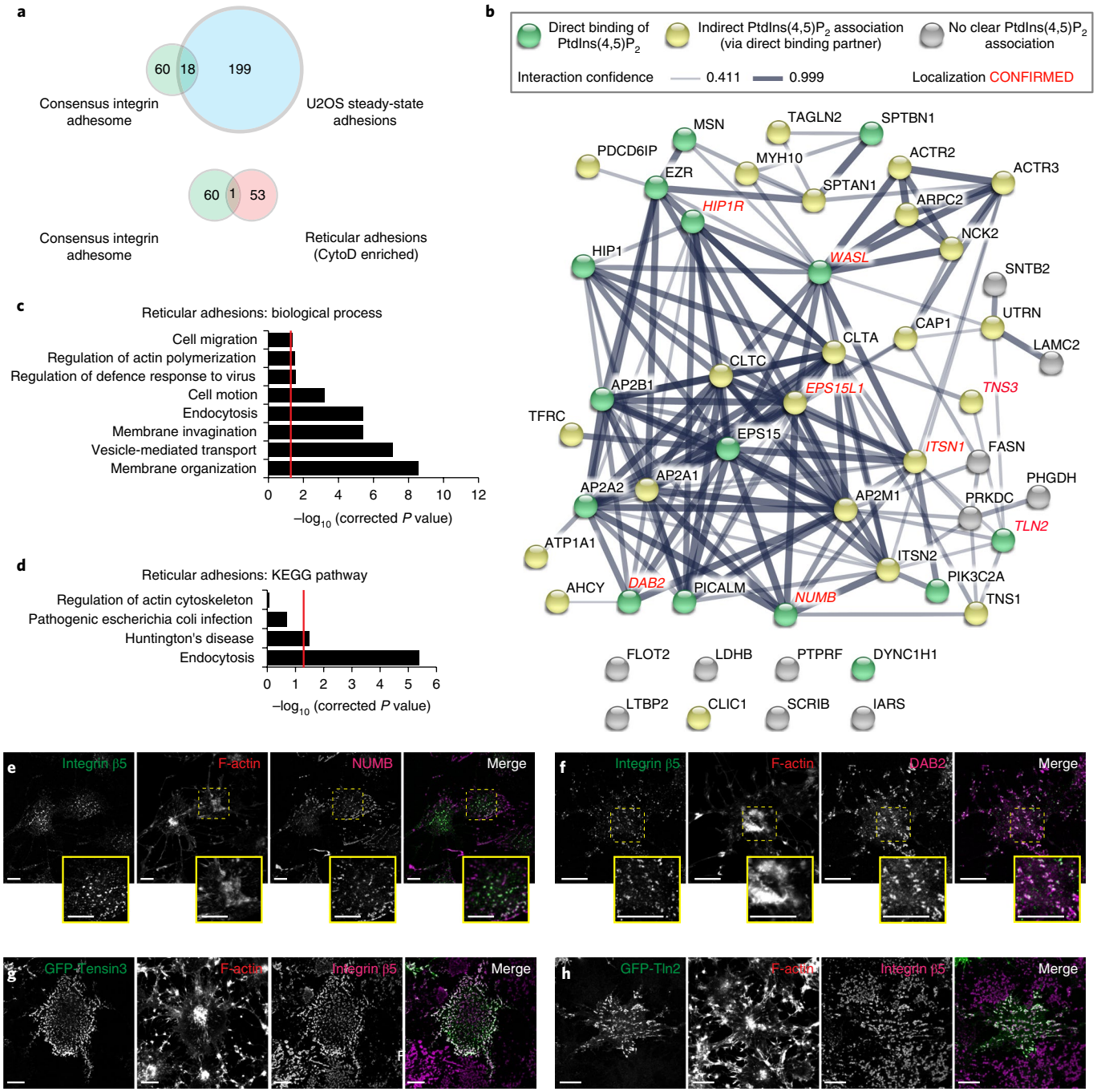

Fig. 5 | Mass spectrometry reveals the distinct reticular adhesome. a, U2OS cells were plated in complete medium for 3 days on tissue culture plastic then treated with either DMSO (steady state) or CytoD (reticular enriched) and MS analysis was performed on the remaining adhesions after cell removal ($n = 3$ biologically independent experiments). The Venn diagrams summarize overlap between proteins identified by MS analysis of ventral membrane preparations isolated from each condition overlaid with the 60 consensus fibronectin-adhesome proteins[5]. **b**, STRING interaction network of reticular adhesion enriched proteins with interaction confidence as indicated. PtdIns(4,5)P_2 binding (direct, green; indirect, yellow; absent, grey) is indicated. **c**,**d**, Gene ontology analysis of reticular adhesion enriched proteins (CytoD-treated) showing terms from Biological Process (**c**) and KEGG pathway analysis (**d**) significantly enriched over whole cell proteome. *P* values were derived from EASE scores calculated using a modified Fishers exact test with Holm–Bonferroni correction from multiple tests using the DAVID annotation system. **e**–**h**, Confocal images of U2OS cells cultured on glass coverslips for 72 h then treated with 20 μM CytoD for 2 h and immuno-labelled against integrin β5 and NUMB (**e**) DAB2 (**f**) or in cells transfected with EGFP-tensin-3 (**g**) or EGFP-talin-2 (**h**); along with staining of F-actin. Images in **e**–**h** are representative of three biologically independent experiments. Scale bars, 10 μm (main images) and 5 μm (magnified regions in **e** and **f**).

The balance between reticular and focal adhesion complexes is shaped by PIP status. The putative reticular adhesion protein interaction network contains many components reported to bind phosphatidylinositol-4,5-bisphosphate (PtdIns(4,5)P_2; Fig. 5b and Supplementary Table 2). In five out of six cases where siRNA-mediated PIP (phosphatidylinositol) regulator depletion would be

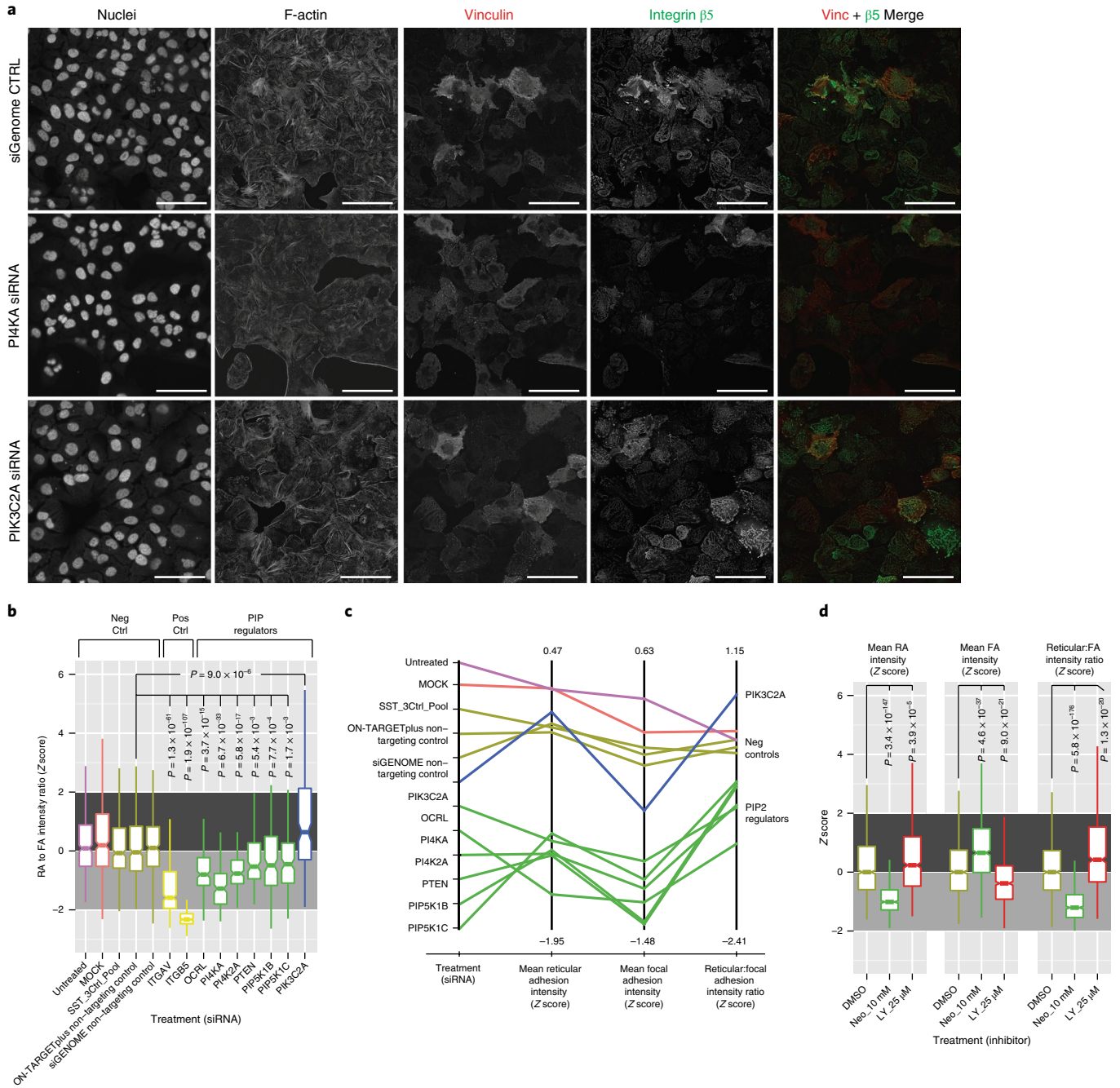

Fig. 6 | Reticular versus focal adhesion balance is shaped by PIP status. a, Representative images illustrating DAPI (nuclei) and F-actin staining as well as localization of mCherry-vinculin and integrin β5-2GFP fluorescence following treatment with control siRNA or siRNAs targeting PI4KA or PIK3C2A. Scale bars, 50 μm. **b**, Boxplots summarizing single cell quantification (from images in **a**; $n = 3{,}917$ cells analysed, averaging 280 ± 131 (s.d.) per condition) of integrin β5 intensity ratios (represented as *Z*-scores) between reticular and focal adhesions following knockdown of various PtdIns(3,4)P_2 and PtdIns(3,4,5)P_3 regulators. Data are derived from two biologically independent experiments. Boxplot centre and box edges indicate median and 25th or 75th percentiles, respectively, and whiskers indicate the median ± 1.5 × IQR or the most extreme observations within these limits. Boxplot notches approximate 95% CI (see Methods for details). *P* values reflect two-sided unpaired Mann–Whitney *U*-testing with Holm–Bonferroni correction from multiple tests. **c**, Parallel coordinates plot displaying (as *Z*-scores) mean focal and reticular adhesion integrin β5 intensities, as well as the ratio of reticular versus focal adhesion intensities, following knockdown of PtdIns(4,5)P_2 and PtdIns(3,4,5)P_3 regulators, based on $n = 3{,}917$ cells analysed, averaging 280 ± 131 (s.d.) per condition. Data are derived from two biologically independent experiments. **d**, Boxplots summarizing single cell quantification (from images as shown in Supplementary Fig. 6b; $n = 3{,}018$ cells analysed, averaging 1,006 ± 307 (s.d.) per condition) of mean focal and reticular adhesion integrin β5 intensity and ratio following 30 min treatment with 10 mM neomycin (PIP2PtdIns(3,4)P_2 binding inhibition) or 25 μM LY294002 (inhibition of PtdIns(3,4,5)P_3 generation). Boxplot features are as detailed above. *P* values reflect two-sided unpaired Mann–Whitney *U*-testing with Holm–Bonferroni correction from multiple tests. Data in **d** are derived from three biologically independent experiments. Source data for **b**–**d** are provided in Supplementary Table 1.

expected to reduce PtdIns(4,5)P_2 levels (PI4KA, PI4K2A, PIP5K1B, PIP5K1C and PTEN), a shift in β5-2GFP intensity ratio was observed from reticular to focal adhesions (Fig. 6a–c and Supplementary Fig. 6a). Correspondingly, depletion of PIK3C2A, which generates phosphatidylinositol-3,4,5-trisphosphate (PtdIns(3,4,5)P_3) from PtdIns(4,5)P_2, caused a relative shift from focal to reticular adhesions. Depletion of targets that produce PtdIns(4,5)P_2 reduced β5-2GFP levels in both adhesion complex types (Fig. 6c), yet, because the effects were more pronounced for reticular adhesions, the ratio to focal adhesions decreased. In contrast, PIK3C2A depletion perturbed only focal adhesions. Neomycin (a PtdIns(4,5)P_2 binding inhibitor) reduced β5-2GFP intensities in reticular adhesions while increasing intensities in focal adhesions (Fig. 6d and Supplementary Fig. 6b). Conversely, LY294002 (a PtdIns(3,4,5)P_3 formation inhibitor) increased reticular adhesion and reduced focal adhesion intensities. These findings indicate that focal and reticular adhesions are in equilibrium, with PtdIns(4,5)P_2 promoting reticular adhesions and PtdIns(3,4,5)P_3 promoting focal adhesions.

Reticular adhesions persist throughout division when focal adhesions disassemble. siRNA-mediated knockdown of integrin β5 reduced cell proliferation (Fig. 7a) without affecting S-phase progression (Fig. 7b). We therefore probed a potential role for β5 in mitosis. Unlike classical adhesion complexes, reticular adhesions persisted throughout division (Fig. 7c–i and Supplementary Movie 6), remaining free of consensus adhesome components (Supplementary Fig. 7a–e). In virtually all cells on purified laminin or fibronectin, where integrin β1 is preferentially engaged (Supplementary Fig. 7f,g), we detected no β1-labelled adhesion complexes during mitosis. β1-containing adhesion complexes were detected during mitosis only in normal human fibroblasts on fibronectin. In other cells, mitotic cells retained adhesion by cell–cell association. These results suggest a selective role for αVβ5 in mitotic cell attachment.

The pre-mitotic footprint of the mother cell is transmitted with high precision to post-mitotic daughter cells (Fig. 7c,d)[31,32]. During the rounding phase of mitosis, this footprint was demarcated by membrane dye-labelled retraction fibres and integrin β5-2GFP-labelled reticular adhesions (Fig. 7c,f,g). The exquisite correspondence between retraction fibres (Fig. 7h) and reticular adhesions (Fig. 7i) was highlighted by 3D visualization of a similarly staged mitotic cell (Fig. 7j–l and Supplementary Movie 7). Here, retraction fibres angled down and attached precisely at sites decorated with β5-labelled reticular adhesions. A role for reticular adhesions in directing post-division cell spreading was also exemplified by live cell imaging (Supplementary Movie 8). Quantitative comparison of focal and reticular adhesions during division confirmed that the number and intensity of vinculin-positive focal adhesions fell to virtually zero during mitosis, while β5-positive reticular adhesion numbers and β5 intensity were maintained (Fig. 7m,n). As previously reported, mitotic retraction fibres contain dense actin filaments (Supplementary Fig. 7h,i and Supplementary Movie 9). We detected weak F-actin signals in reticular adhesions at the tips of mitotic retraction fibres (Supplementary Fig. 7h–k), with F-actin concentrations well below those within the retraction fibres, suggesting that reticular adhesions have limited coupling to F-actin following mitotic cell rounding or that retraction fibres function via membrane tension and mediate adhesion independent of F-actin.

Reticular adhesions are required for division and inter-generational spatial memory transmission. A detailed comparison of reticular adhesion distributions before, during and after mitosis (Fig. 8a–c and Supplementary Movie 10) indicated that the overall geometry of central reticular adhesions remained virtually unchanged between generations, providing a potential mechanism for spatial memory storage. In contrast, peripheral reticular adhesions (generally associated with mitotic retraction fibres) underwent significant remodelling characterized by both narrowing and intensification of the complex (Fig. 8d). Nanoscale STORM imaging confirmed that central mitotic reticular adhesions were indistinguishable in nano-organization from interphase reticular adhesions (Fig. 3g–i versus Fig. 8d–f), while peripheral mitotic retraction fibre-associated reticular adhesions were linearized and condensed. This was confirmed by quantification of nanocluster nearest-neighbour distances and molecular localization counts per nanocluster (Fig. 8e,f). Such molecular-scale remodelling functionally implicates reticular adhesions in the mechanical process of cell–ECM attachment during division.

Many cells exhibit a preference to divide along the major axis of the pre-mitotic mother cell, thus determining the spatial arrangement of daughter cells[8–11]. We therefore measured the residual angle between the pre-mitotic major axis and the mitotic division axis in HeLa cells (Fig. 8g,h), chosen for their expression of reticular adhesions (Supplementary Fig. 1b) and their extensive mitotic characterization[33]. Residual angle distributions were skewed towards zero (indicating spatial memory retention) in control cells and β5-rescued cells. By contrast, mitotic axis orientation in integrin-β5-depleted cells was almost random relative to the pre-mitotic major axis, indicating a loss of spatial memory. Thus, reticular adhesions are required for intergenerational spatial memory transmission during division.

Only 20% of β5-depleted cells underwent normal division, versus 75% for controls (Fig. 8i). A range of defects were observed in β5-depleted cells, including delayed mitosis (often with incomplete cytokinesis), repeated cell rounding and re-spreading without division, and failure of cytokinesis resulting in binucleate daughter cells (Supplementary Fig. 8a,b and Supplementary Movies 11–14). The frequency of these errors[34] was reduced by β5-EGFP rescue (Fig. 8i, Supplementary Fig. 8c,d and Supplementary Movie 15). Together, these findings demonstrate that integrin β5-mediated reticular adhesions are essential for normal progression of division in HeLa cells.

Discussion

Here, we report the identification and characterization of a previously unrecognized cellular structure, the reticular adhesion, an adhesion complex mediating cell–ECM attachment during mitosis. Reticular adhesions form in a diverse array of cell types and are characterized by both the presence of integrin αVβ5 and the absence of consensus adhesome components. Furthermore, in contrast to focal adhesions, reticular adhesions can form independently of F-actin and talin.

Reticular adhesions persist throughout mitosis and provide a solution to the paradox of mitotic cell–ECM adhesion, which endures despite the absence of all previously known adhesion complexes[13,15,18]. Cell–ECM attachment is essential for spatial memory transmission between cell generations, including defining the axis of division[8–11]and facilitating cytokinesis[35–37]. So far, it has been unclear how residual adhesion is maintained during mitosis, how mitotic retraction fibres[38] are tethered to the substratum, and how re-spreading is guided thereafter. Reticular adhesions now provide mechanisms underpinning all these phenomena. The unique characteristics of reticular adhesions appear suited to these roles in division. For instance, F-actin independence decouples reticular adhesions from large-scale cytoskeletal remodelling during cell rounding, while the ability to interact with membrane retraction fibres is maintained. This key role for reticular adhesions in division is confirmed by integrin β5 depletion, which causes multiple mitotic defects and disturbed spatial memory transmission.

While we find an important role for αVβ5 during division, cells can also proliferate on ECM ligands not engaging αVβ5. This implies that cells can deploy alternative adhesion receptors for mitotic anchorage. For example, integrin α6β4-positive hemides-

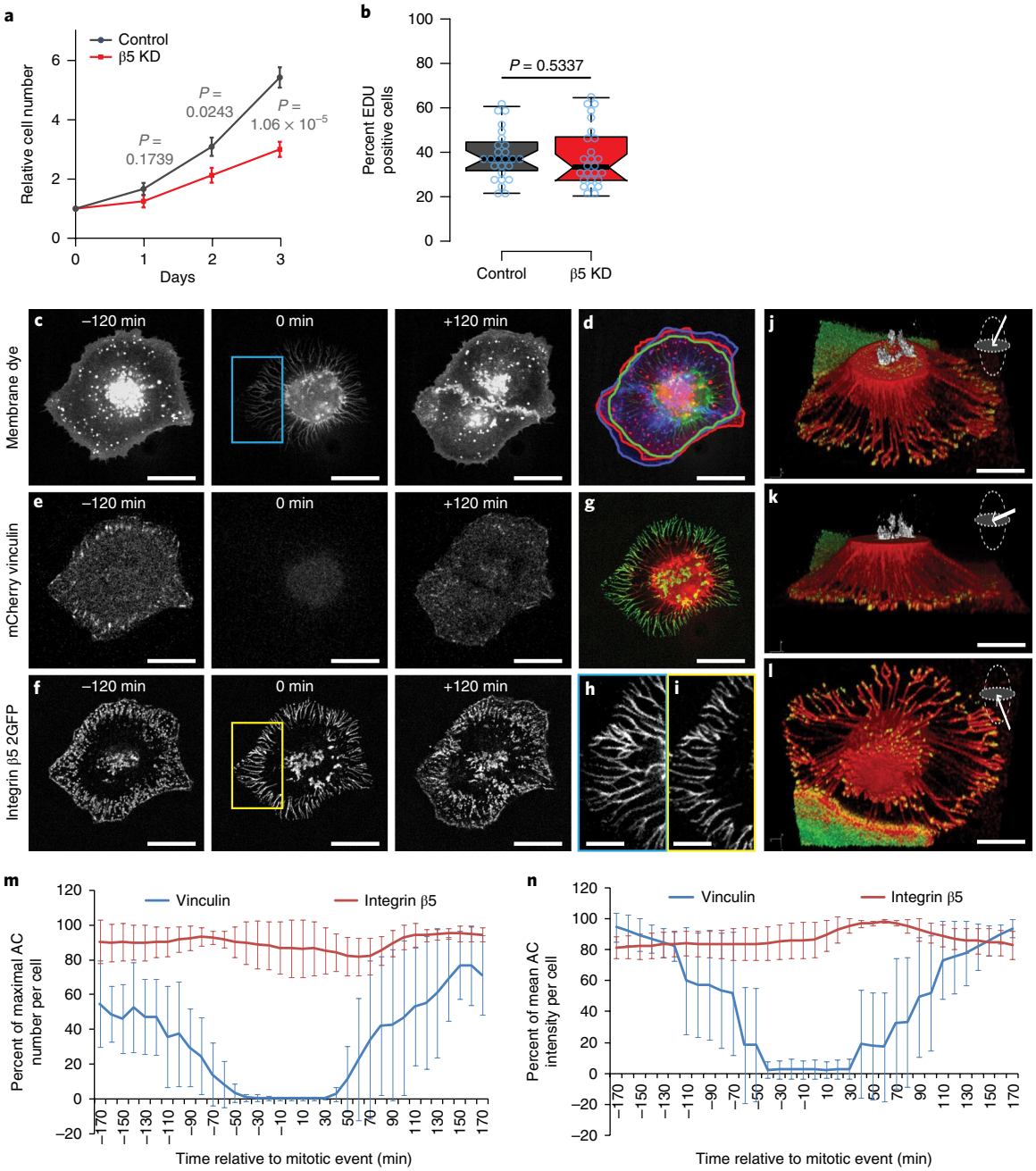

Fig. 7 | Reticular adhesions persist during mitosis and transmit spatial memory from pre-mitotic to post-mitotic daughter cells. a,**b**, Proliferation of control or integrin β5 knockdown U2OS cells over 3 days post attachment: mean ± s.d. of $n = 14$ replicates across three biologically independent experiments; *P* values reflect two-sided unpaired *t*-testing relative to day zero (**a**); percentage of EdU-positive cells 3 days post attachment for $n = 26$ fields of view containing 55–217 cells each across three biologically independent experiments, with distribution of individual values in blue rings (**b**). Boxplot centre and box edges indicate median and 25th or 75th percentiles, respectively, whiskers indicate median ± 1.5 × IQR or the most extreme observations within these limits. Boxplot notches approximate 95% CIs. *P* values reflect two-sided unpaired *t*-testing for Control versus β5-KD. **c**,**e**–**g**, U2OS cells labelled with far-red membrane dye (**c**) and expressing mCherry-vinculin (**e**) and integrin β5-2GFP (**f**), replated on vitronectin and imaged every 10 min via spinning-disc confocal microscopy during mitosis (Supplementary Movie 6). Images show a cell 120 min before, during (merged in **g**) and 120 min after mitosis. **d**, Overlay of membrane labelling with cell boundaries outlined at −120 min (red), 0 min (green) and +120 min (blue), highlighting recovery of the pre-mitotic adhesion footprint by daughter cells. **h**,**i**, Membranous retraction filaments formed during mitosis (**h**, cropped from blue region of interest in **c**) overlap exactly with integrin β5-2GFP-positive adhesion complexes (**i**, cropped from yellow region of interest in **f**). Scale bars, 10 µm (**c**–**g**) and 5 µm (**h**,**i**). (**j**–**l** derived from Supplementary Movie 7.) **j**–**l**, Three alternative views (above, **j**; beside, **k**; below, **l**; orientation indicated by arrows in planar schematics) of a 3D confocal-reconstructed mitotic cell showing condensed DNA (white), cell membrane labelling (red; cut through to expose DNA) and integrin β5-2GFP labelling of reticular adhesions (green). Images in **c**–**l** are representative of five biologically independent experiments. **m**,**n**, Quantification of vinculin-positive adhesion complex (AC) number (**m**, blue) and intensity (**n**, blue) versus β5-2GFP-positive adhesion complex number (**m**, red) and intensity (**n**, red) during mitosis. Mean values from $n = 5$ cells are shown ± s.d., derived from three biologically independent experiments. Source data for **a**, **b**, **m** and **n** are provided in Supplementary Table 1.

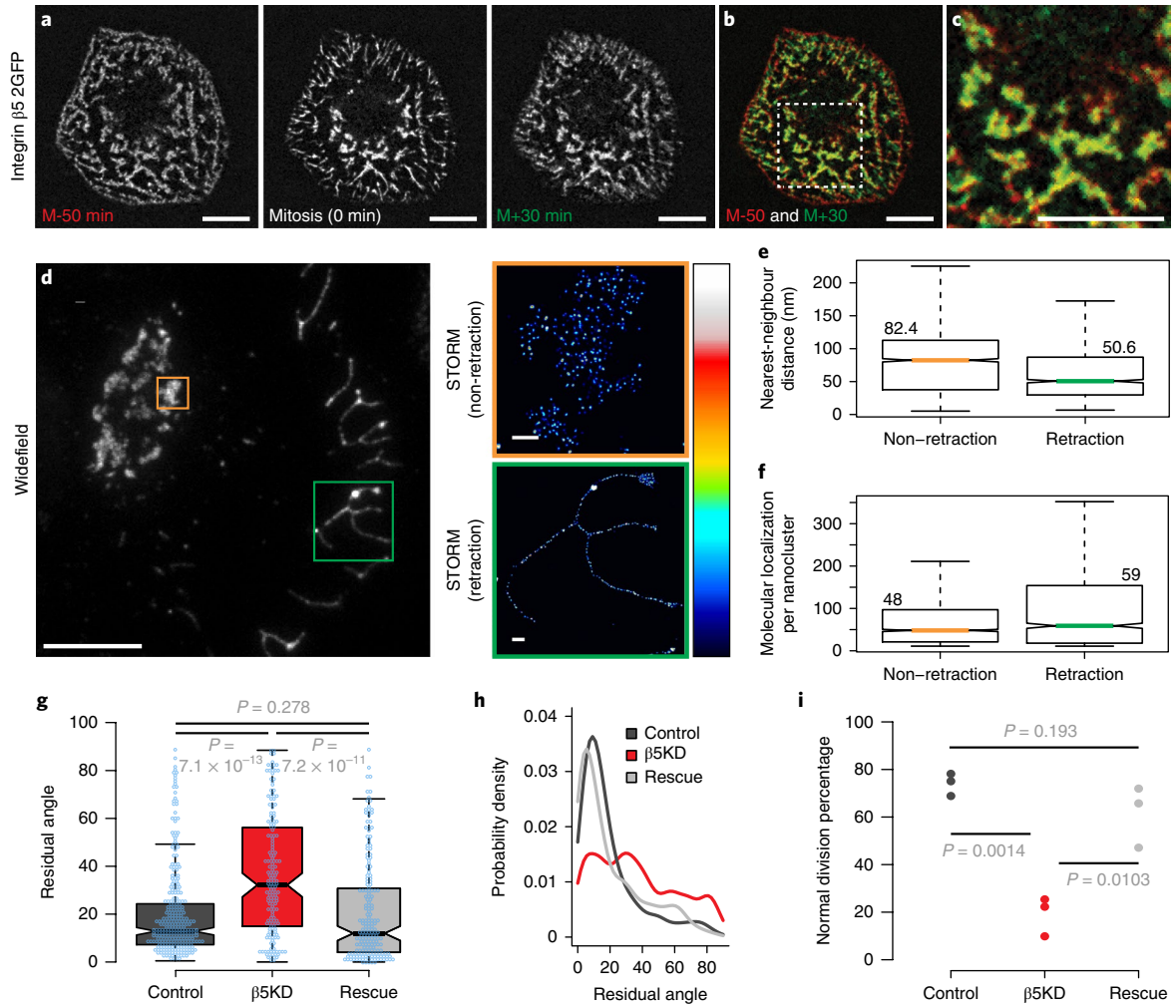

Fig. 8 | Requirement of reticular adhesions for mitosis and post-mitotic re-spreading. a–c, Confocal images of integrin β5-2GFP adhesions at three time points relative to mitosis (−50 min (pre), 0 min, +30 min (post)). **b**,**c**, Overlay of pre- and post-mitosis adhesions (**b**), cropped and magnified in **c**, confirming the persistence of reticular adhesions throughout mitosis (Supplementary Movie 9). Images in **a–c** are representative of at least $n = 5$ biologically independent experiments. **d**, Left, Integrin β5 in a representative U2OS mitotic cell plated on VN and imaged via conventional TIRF microscopy. Right, Representative central (non-retraction, orange box) and peripheral (retraction, green box) reticular adhesions cropped from matched conventional and STORM ('royal' look-up table intensity-scaled as in the legend) images. **e**,**f**, Quantification of integrin β5 nanocluster nearest-neighbour distances (**e**) and molecular localization counts per nanocluster (**f**) based on STORM data. In total, 95 retraction and 83 non-retraction mitotic reticular adhesions were quantified, including $n = 3{,}512$ nanoclusters across two biologically independent experiments. Boxplot centre and box edges indicate median and 25th or 75th percentiles, respectively, while whiskers indicate median ± 1.5 × IQR or the most extreme observations within these limits. Boxplot notches approximate 95% CIs. Scale bars, 10 μm (**a–c** and **d**, left) and 500 nm (**d**, right). **g–i**, Comparison between control siRNA (Control; $n = 297$ cells) and integrin β5 knockdown (β5 KD; $n = 176$ cells) or post-knockdown β5 rescue (Rescue; $n = 195$ cells) effects on spatial memory transmission between HeLa cell generations, defined by residual angle measurement between the pre-mitotic cell major axis and the cell division axis (data derived from two biologically independent experiments). Boxplots (**g**, blue rings indicate individual cell measurements) and probability density plots (**h**) indicate the distribution of residual angles. Boxplot centre and box edges indicate median and 25th or 75th percentiles, respectively, while whiskers indicate the median ± 1.5 × IQR or the most extreme observations within these limits. Boxplot notches approximate 95% CIs. *P* values reflect two-sided unpaired Mann–Whitney *U*-testing. (Based on Supplementary Fig. 8 and Supplementary Movies 10–14.) **i**, Plots showing the percentage of rounding cells that progressed through normal cell division in each of $n = 3$ biologically independent experiments. *P* values reflect two-sided unpaired *t*-testing. Source data for **e–i** are provided in Supplementary Table 1.

mosomes persist through mitosis[39,40] and, despite disassembly of precursor focal adhesion complexes and loss of consensus adhesome components, residual clusters of integrin β1 continue to decorate the cell–ECM interface in mitotic retinal pigment epithelial cells[41]. These β1 integrin clusters differ from reticular adhesions because they are remnants of disassembled focal adhesions, while reticular adhesions represent a distinct adhesion complex population during both interphase and mitosis. Nonetheless, investigation of mitotic adhesion roles for alternative integrins, and their relationship to reticular adhesions, is now merited. The limited phenotype of β5 knockout mice suggests redundancy of function among adhesion receptors and/or a specialized role for αVβ5 in regulating division within specific ECM environments. Both β5 knockout[42] and overexpression[43] in mice cause deficiencies in osteoblast/osteoclast function, potentially reflecting mitotic defects related to differentiation errors[12] in cells on rigid, RGD-rich substrates. Indeed, these environments may be analogous to long-term cell culture conditions, where we show that cells preferentially utilize integrin αVβ5. As αVβ5

is expressed at high levels in a number of proliferative diseases, this raises the possibility that it promotes disease progression by enhancing division within specific ECM environments. It is now important to determine the role of αVβ5 and reticular adhesions in vivo, within physiological and disease settings. In this context, a focal adhesion-independent role for αvβ5 in three-dimensional skin formation and tumour invasion has been reported[44].

Remarkably, reticular adhesions have remained uncharacterized, although early studies reported similar reticular αvβ5 labelling patterns in cells spread on vitronectin [45]. The experimental induction of morphologically comparable structures, such as through manganese- or talin-head-mediated activation of αVβ3 (refs [28,29]), suggests the potential for other integrins to form similar structures given modulation of their activity state. Reticular adhesions lack not only F-actin, but virtually all consensus adhesome components. Most notably, both talin-1 and kindlin are absent, despite being considered necessary and ubiquitous integrin activators[46]. Moreover, perturbations of talin and F-actin indicate that reticular adhesions can form independently of these proteins.

Proteomic analysis of reticular adhesions identified a distinct adhesome, highly enriched in PtdIns(4,5)P_2-binding proteins. These include clathrin-mediated endocytosis adaptors, such as Dab2 and Numb, previously shown to interact directly with the integrin β5 cytoplasmic tail in vitro[47]. These data are consistent with recent evidence of integrin-mediated ECM attachment via clathrin-coated structures[48,49]. Indeed, integrin β5 can localize within clathrin plaques[48,50–52] that are postulated to associate with areas of strong adhesion[34,53–56]. It will be important to determine whether reticular adhesions associate with clathrin lattices to facilitate this adhesion and whether clathrin structures remain associated with the substratum during mitosis. Given that both reticular adhesions and clathrin-coated structures can form in the absence of talin, it follows that some integrins may not depend on talin for their activation[49]. In this context, it is also notable that we observe near identical nanoscale integrin β5 clustering between talin-1-positive and -negative adhesion complexes during interphase, despite previous suggestions that talin-1 determines nanoscale integrin organization[6]. Thus, both in terms of integrin activation and organization, it is possible that either alternative proteins can replace talin-1 functions in reticular adhesions, or that β5 ligand-binding and nanoscale organization are independent of cytosolic regulators. Regardless, the composition, regulation and function of integrin-mediated adhesion complexes appear more diverse than previously recognized.

In conclusion, we have defined reticular adhesions, an overlooked cellular structure and adhesion complex class. Functionally, by mediating cell–ECM attachment during mitosis, reticular adhesions provide a distinctive solution to the paradox of mitotic cell attachment, where classical adhesion complexes must disassemble but cells must also remain adherent. These discoveries not only delineate a specific form of adhesion complex, but also highlight areas of adhesion biology that merit further attention, including the integrins and adhesion complexes employed in vivo.

Online content

Any methods, additional references, Nature Research reporting summaries, source data, statements of data availability and associated accession codes are available at https://doi.org/10.1038/s41556-018-0220-2.

Received: 14 December 2017; Accepted: 21 September 2018;
Published online: 22 October 2018

References

1. Lock, J. G., Wehrle-Haller, B. & Strömblad, S. Cell-matrix adhesion complexes: master control machinery of cell migration. *Semin. Cancer Biol.* **18**, 65–76 (2008).
2. Hynes, R. O. Integrins: bidirectional, allosteric signaling machines. *Cell* **110**, 673–687 (2002).
3. Berrier, A. L. & Yamada, K. M. Cell-matrix adhesion. *J. Cell. Physiol.* **213**, 565–573 (2007).
4. Horton, E. R. et al. Definition of a consensus integrin adhesome and its dynamics during adhesion complex assembly and disassembly. *Nat. Cell Biol.* **17**, 1577–1587 (2015).
5. Tadokoro, S. et al. Talin binding to integrin β tails: a final common step in integrin. *Science* **302**, 103–106 (2008).
6. Liu, J. et al. Talin determines the nanoscale architecture of focal adhesions. *Proc. Natl Acad. Sci. USA* **112**, E4864–E4873 (2015).
7. Gardel, M. L., Schneider, I. C., Aratyn-Schaus, Y. & Waterman, C. M. Mechanical integration of actin and adhesion dynamics in cell migration. *Annu. Rev. Cell Dev. Biol.* **26**, 315–333 (2010).
8. Jime, A. et al. Experimental and theoretical study of mitotic spindle orientation. *Nature* **447**, 493–496 (2007).
9. Théry, M. et al. The extracellular matrix guides the orientation of the cell division axis. *Nat. Cell Biol.* **7**, 947–953 (2005).
10. Théry, M., Jiménez-Dalmaroni, A., Racine, V., Bornens, M. & Jülicher, F. Experimental and theoretical study of mitotic spindle orientation. *Nature* **447**, 493–496 (2007).
11. Théry, M. & Bornens, M. Cell shape and cell division. *Curr. Opin. Cell Biol.* **18**, 648–657 (2006).
12. Akanuma, T., Chen, C., Sato, T., Merks, R. M. H. & Sato, T. N. Memory of cell shape biases stochastic fate decision-making despite mitotic rounding. *Nat. Commun.* **7**, 11963 (2016).
13. Maddox, A. S. & Burridge, K. RhoA is required for cortical retraction and rigidity during mitotic cell rounding. *J. Cell Biol.* **160**, 255–265 (2003).
14. Lancaster, O. et al. Mitotic rounding alters cell geometry to ensure efficient bipolar spindle formation. *Dev. Cell* **25**, 270–283 (2013).
15. Dao, V. T., Dupuy, A. G., Gavet, O., Caron, E. & de Gunzburg, J. Dynamic changes in Rap1 activity are required for cell retraction and spreading during mitosis. *J. Cell Sci.* **122**, 2996–3004 (2009).
16. Petridou, N. I. & Skourides, P. A. A ligand-independent integrin β1 mechanosensory complex guides spindle orientation. *Nat. Commun.* **7**, 10899 (2016).
17. LaFlamme, S. E., Nieves, B., Colello, D. & Reverte, C. G. Integrins as regulators of the mitotic machinery. *Curr. Opin. Cell Biol.* **20**, 576–582 (2008).
18. Ramkumar, N. & Baum, B. Coupling changes in cell shape to chromosome segregation. *Nat. Rev. Mol. Cell Biol.* **17**, 511–521 (2016).
19. Winograd-Katz, S. E., Fässler, R., Geiger, B. & Legate, K. R. The integrin adhesome: from genes and proteins to human disease. *Nat. Rev. Mol. Cell Biol.* **15**, 273–288 (2014).
20. Hernández-Varas, P., Berge, U., Lock, J. G. & Strömblad, S. A plastic relationship between vinculin-mediated tension and adhesion complex area defines adhesion size and lifetime. *Nat. Commun.* **6**, 7524 (2015).
21. Lock, J. G. et al. Plasticity in the macromolecular-scale causal networks of cell migration. *PLoS ONE* **9**, e90593 (2014).
22. Ballestrem, C., Hinz, B., Imhof, B. A. & Wehrle-Haller, B. Marching at the front and dragging behind: differential αVβ3-integrin turnover regulates focal adhesion behavior. *J. Cell Biol.* **155**, 1319–1332 (2001).
23. Besser, A. & Safran, S. A. Force-induced adsorption and anisotropic growth of focal adhesions. *Biophys. J.* **90**, 3469–3484 (2006).
24. Yu, C. H. et al. Integrin-matrix clusters form podosome-like adhesions in the absence of traction forces. *Cell Rep.* **5**, 1456–1468 (2013).
25. Mohl, C., Kirchgessner, N., Schafer, C., Hoffmann, B. & Merkel, R. Quantitative mapping of averaged focal adhesion dynamics in migrating cells by shape normalization. *J. Cell Sci.* **125**, 155–165 (2012).
26. Spiess, M. et al. Active and inactive β1 integrins segregate into distinct nanoclusters in focal adhesions. *J. Cell Biol.* **217**, 1929–1940 (2018).
27. Zhang, X. et al. Talin depletion reveals independence of initial cell spreading from integrin activation and traction. *Nat. Cell Biol.* **10**, 1062–1068 (2008).
28. Cluzel, C. et al. The mechanisms and dynamics of αvβ3 integrin clustering in living cells. *J. Cell Biol.* **171**, 383–392 (2005).
29. Saltel, F. et al. New PI(4,5)P2- and membrane proximal integrin-binding motifs in the talin head control β3-integrin clustering. *J. Cell Biol.* **187**, 715–731 (2009).
30. Mellacheruvu, D. et al. The CRAPome: a contaminant repository for affinity purification-mass spectrometry data. *Nat. Methods* **10**, 730–736 (2013).
31. Toyoshima, F. & Nishida, E. Integrin-mediated adhesion orients the spindle parallel to the substratum in an EB1- and myosin X-dependent manner. *EMBO J.* **26**, 1487–1498 (2007).
32. Mali, P., Wirtz, D. & Searson, P. C. Interplay of RhoA and motility in the programmed spreading of daughter cells postmitosis. *Biophys. J.* **99**, 3526–3534 (2010).
33. Held, M. et al. CellCognition: time-resolved phenotype annotation in high-throughput live cell imaging. *Nat. Methods* **7**, 747–754 (2010).

34. Maupin, P. & Pollard, T. D. Improved preservation and staining of HeLa cell actin filaments, clathrin-coated membranes, and other cytoplasmic structures by tannic acid-glutaraldehyde-saponin fixation. *J. Cell Biol.* **96**, 51–62 (1983).
35. Aszodi, A., Hunziker, E. B., Brakebusch, C. & Fässler, R. β1 integrins regulate chondrocyte rotation, G1 progression, and cytokinesis. *Genes Dev.* **17**, 2465–2479 (2003).
36. Thullberg, M., Gad, A., Le Guyader, S. & Strömblad, S. Oncogenic H-Ras V12 promotes anchorage-independent cytokinesis. *Proc. Natl Acad. Sci. USA* **104**, 20338–20343 (2007).
37. Reverte, C. G., Benware, A., Jones, C. W. & LaFlamme, S. E. Perturbing integrin function inhibits microtubule growth from centrosomes, spindle assembly, and cytokinesis. *J. Cell Biol.* **174**, 491–497 (2006).
38. Cramer, L. P. & Mitchison, T. J. Investigation of the mechanism of retraction of the cell margin and rearward flow of nodules during mitotic cell rounding. *Mol. Biol. Cell* **8**, 109–119 (1997).
39. Riddelle, K. S., Hopkinson, S. B. & Jones, J. C. Hemidesmosomes in the epithelial cell line 804G: their fate during wound closure, mitosis and drug induced reorganization of the cytoskeleton. *J. Cell Sci.* **103**, 475–490 (1992).
40. Baker, J. & Garrod, D. Epithelial cells retain junctions during mitosis. *J. Cell Sci.* **104**, 415–425 (1993).
41. Dix, C. L. et al. The role of mitotic cell-substrate adhesion re-modeling in animal cell division. *Dev. Cell* **45**, 132–145 (2018).
42. Lane, N. E. et al. Mice lacking the integrin β5 subunit have accelerated osteoclast maturation and increased activity in the estrogen-deficient state. *J. Bone Miner. Res.* **20**, 58–66 (2005).
43. Coudert, A. E. et al. Differentially expressed genes in autosomal dominant osteopetrosis type II osteoclasts reveal known and novel pathways for osteoclast biology. *Lab. Invest.* **94**, 275–285 (2014).
44. Duperret, E. K., Dahal, A. & Ridky, T. W. Focal-adhesion-independent integrin-v regulation of FAK and c-Myc is necessary for 3D skin formation and tumor invasion. *J. Cell Sci.* **128**, 3997–4013 (2015).
45. Wayner, E. A., Orlando, R. A. & Cheresh, D. A. Integrins αvβ3 and αvβ5 contribute to cell attachment to vitronectin but differentially distribute on the cell surface. *J. Cell Biol.* **113**, 919–929 (1991).
46. Klapholz, B. & Brown, N. H. Talin—the master of integrin adhesions. *J. Cell Sci.* **130**, 2435–2446 (2017).
47. Calderwood, D. A. et al. Integrin β cytoplasmic domain interactions with phosphotyrosine-binding domains: a structural prototype for diversity in integrin signaling. *Proc. Natl Acad. Sci. USA* **100**, 2272–2277 (2003).
48. Leyton-Puig, D. et al. Flat clathrin lattices are dynamic actin-controlled hubs for clathrin-mediated endocytosis and signalling of specific receptors. *Nat. Commun.* **8**, 16068 (2017).
49. Elkhatib, N. et al. Tubular clathrin/AP-2 lattices pinch collagen fibers to support 3D cell migration. *Science* **356**, eaal4713 (2017).
50. De Deyne, P. G. et al. The vitronectin receptor associates with clathrin-coated membrane domains via the cytoplasmic domain of its β5 subunit. *J. Cell Sci.* **111**, 2729–2740 (1998).
51. Vassilopoulos, S. et al. Actin scaffolding by clathrin heavy chain is required for skeletal muscle sarcomere organization. *J. Cell Biol.* **205**, 377–393 (2014).
52. Papoulas, O., Hays, T. S. & Sisson, J. C. The golgin lava lamp mediates dynein-based Golgi movements during *Drosophila* cellularization. *Nat. Cell Biol.* **7**, 612–618 (2005).
53. Akisaka, T., Yoshida, H., Suzuki, R., Shimizu, K. & Takama, K. Clathrin sheets on the protoplasmic surface of ventral membranes of osteoclasts in culture. *J. Electron Microscop.* **52**, 535–543 (2003).
54. Saffarian, S., Cocucci, E. & Kirchhausen, T. Distinct dynamics of endocytic clathrin-coated pits and coated plaques. *PLoS Biol.* **7**, e1000191 (2009).
55. Nicol, A. & Nermut, M. A new type of substratum adhesion structure in NRK cells revealed by correlated interference reflection and electron microscopy. *Eur. J. Cell Biol.* **43**, 348–357 (1987).
56. Akisaka, T., Yoshida, H., Suzuki, R. & Takama, K. Adhesion structures and their cytoskeleton-membrane interactions at podosomes of osteoclasts in culture. *Cell Tissue Res.* **331**, 625–641 (2008).

Acknowledgements

The authors thank D. Critchley (University of Leicester) for providing talin-1-null embryonic stem cells and Z. Li for assistance with the integrin β5/β3-EGFP construct. This work was supported by grants to S.S. from the EU-FP7-Systems Microscopy Network of Excellence (HEALTH-F4-2010-258068), EU-H2020-Multimot (EU grant agreement no. 634107), the Strategic Research Foundation of Sweden (SB16-0046), the Swedish Research Council (521-2012-3180) and the Swedish Cancer Society, and by a grant to M.J.H. from Cancer Research UK (grant no. 13329/A21671). Imaging was in part performed at the live cell imaging facility and Nikon Center of Excellence at the Department of Biosciences and Nutrition, Karolinska Institutet, supported by grants from the Knut and Alice Wallenberg Foundation, the Swedish Research Council, the Centre for Innovative Medicine and the Jonasson donation to the School of Technology and Health, Royal Institute of Technology, Sweden. The authors also acknowledge support from the Bioimaging and Bio-MS core facilities at the University of Manchester. The mass spectrometers and microscopes used in this study were purchased with grants from BBSRC, Wellcome Trust and the University of Manchester Strategic Fund. The funders had no role in study design, data collection and analysis, decision to publish or preparation of the manuscript. J.A.A. and X.G. contributed equally to this paper.

Author contribution

J.G.L., M.C.J., J.A.A., M.L., M.J.H. and S.S. conceived the project and devised experiments. J.G.L. and J.A.A. performed live cell imaging and related image analyses. J.G.L., M.C.J., J.A.A., X.G. and H.O. performed fixed cell imaging. X.G. performed the siRNA screening for PIP regulators. M.C.J. and J.A.A. undertook experiments relating to integrin β5 RNAi and MS analyses. A.O. performed STORM imaging and related image analyses. H.O. and S.G. performed immunoblotting. J.L. performed image analyses, statistical analyses and data visualization. J.G.L., M.C.J., J.A.A., X.G., M.L., M.J.H. and S.S. contributed to writing the manuscript.

Competing interests

The authors declare no competing interests.

Additional information

Supplementary information is available for this paper at https://doi.org/10.1038/s41556-018-0220-2.

Reprints and permissions information is available at www.nature.com/reprints.

Correspondence and requests for materials should be addressed to J.G.L. or S.S.

Publisher's note: Springer Nature remains neutral with regard to jurisdictional claims in published maps and institutional affiliations.

Methods

Cell culture, plasmid generation, transfection and stable cell generation. *Cell culture.* U2OS human osteosarcoma cells (ATCC), HeLa human cervical carcinoma cells (ECACC), MCF-7 human breast carcinoma cells (ATCC), A549 human lung carcinoma cells (ECACC) and A375 human melanoma cells (ECACC) were maintained in DMEM (Gibco) supplemented with 10% FBS (Sigma) and 2 mM L-glutamine (Gibco). U2OS-β5V cells stably expressing integrin β5-2GFP and mCherry-vinculin were maintained with the addition of 600 μg ml^{-1} geneticin (G-418 sulfate; Gibco). H1299 human non-small lung cancer cells (gift from B. Geiger, The Weizmann Institute of Science) and CS-1 wild-type hamster melanoma cells were cultured in RPMI-1640 (Gibco) medium supplemented with 10% FBS and 5 mg ml^{-1} L-glutamine. CS-1 cells stably expressing integrin β5 (CS1-β5) were maintained with the addition of 500 μg ml^{-1} G-418. BT549 (ductal breast carcinoma, ATCC) cells were maintained in RPMI 1640 medium containing 10% FBS and 1 mM L-glutamine. MAE cells (ATCC) were grown in RPMI 1640 medium with 5% FBS. Human hTERT immortalized retinal pigment epithelial ((hTERT-RPE1) cells (gift from J. Mansfeld, University of Dresden) were cultured in DMEM/F12 (Gibco) supplemented with 10% FBS and 2 mM L-glutamine. Normal human dermal fibroblasts (NHDFs) (Biowhittaker) were grown in DMEM (Gibco) supplemented with 10% FBS (Sigma) and hTERT-human microvascular endothelial cells (HME1) (ATCC) were grown in MEGM (Lonza) supplemented with MEGM BulletKit (Lonza). All live cells were incubated and imaged in a humidified environment at 37 °C with 5% CO_2.

DNA plasmid generation and sourcing. For construction of integrin β5-2GFP, EGFP was duplicated in a pEGFP-N1 backbone vector (gift of P. Caswell, University of Manchester), then a full-length integrin β5 cDNA (gift of E. Ruoslahti, Burnham Institute) was subcloned into the 2XEGFP-N1 vector using the EcoRI site of the original pEGFP-N1 vector. The mCherry-vinculin plasmid was provided by V. Small (IMBA). Csk-GFP was provided by A. Imamoto (University of Chicago). GFP-Tensin3 was provided by P. Caswell (University of Manchester) and GFP-talin2 was provided by B. Goult (University of Kent). RFP-talin1 Head and Rod constructs were provided by M. Parsons (King's College). LifeAct-RubyRed was provided by R. Wedlich-Soldner (Max-Planck Institute for Biochemistry).

Transfection and stable cell line generation. Cells were transfected at 70–90% confluence, 24 h after plating into 12-well culture plates (except where otherwise stated). For DNA plasmid transfection, 0.3–2 μg of total DNA was mixed with 0.5–3 μl of Lipofectamine Plus or Lipofectamine 2000 (Thermo Fisher Scientific) according to the manufacturer's instructions. For RNA transfection, except where otherwise stated, 15–30 pmol of siRNA was transfected together with 0.5–3 μl of RNAiMAX (Thermo Fisher Scientific). Cells were typically imaged 24–48 h after transfection. U2OS-β5V cells expressing integrin β5-2GFP and mCherry-vinculin were established via manual single colony selection followed by selection with 600 μg ml^{-1} G-418.

ECM surface coating. Cells were typically assayed in 96-well glass-bottomed plates (0.17 mm optical glass; Matrical Bioscience). Glass coating was performed at 37 °C for 2 h after blocking with 1% heat-denatured bovine serum albumin (BSA; Sigma-Aldrich) for 2 h at 37 °C. ECM ligand coating concentrations were 10 μg ml^{-1} except where otherwise indicated. Vitronectin and fibronectin were purified from human plasma as detailed previously[57,58], while purified laminin was acquired commercially (Sigma-Aldrich).

Antibodies, immunofluorescence labelling and immunoblotting. Primary antibodies used for immunofluorescence and/or immunoblotting are summarized in Supplementary Table 4 and include anti-integrin αVβ5 (15F11; MAB2019Z; Millipore), anti-integrin αVβ5 (P1F6; Abcam), polyclonal (rabbit) anti-integrin β5 (ab15459; Abcam), anti-integrin β5 (4708S; Cell Signalling Technology), anti-integrin αV (LM142; Merck Millipore), anti-talin2 (53.8; BioRad), anti-talin (8d4; Sigma Aldrich), anti-talin 1 (TA205; Santa Cruz), anti-talin-2 (68E7; Abcam), anti-integrin αVβ3 (LM609; Abcam), anti-integrin β3 (AP3; Abcam), anti-integrin β1 (LM534; Millipore), anti-vinculin (hVIN-1; Sigma-Aldrich), anti-vinculin (V9131; Sigma-Aldrich), anti-intersectin 1 (HPA018007; Atlas Antibodies, Sigma-Aldrich), anti-NUMB (2733; Cell Signaling Technologies), anti-EPS15L1 (HPA055309; Atlas Antibodies, Sigma-Aldrich), anti-HIP1 (HPA013606; Atlas Antibodies, Sigma-Aldrich), anti-WASL (HPA005750; Atlas Antibodies, Sigma-Aldrich), anti-DAB2 (12906; Cell Signaling Technologies), anti-paxillin (5H11; Sigma-Aldrich), anti-FAK (BD Biosciences), anti-zyxin (H-200; Santa Cruz), anti-kindlin 2 (ab74030; Abcam), anti-ICAP1 (115228; Abcam), anti-DOK1 (HPA048561; Atlas Antibodies, Sigma-Aldrich), polyclonal (rabbit) anti-phosphotyrosine (1000) (Cell Signaling), anti-cytokeratin (27988; Abcam) anti-α-tubulin (DM1A; Thermo Fisher Scientific), anti-vimentin (8978; Abcam) and anti-ARP3 (ab49671; abcam). Anti-mouse and anti-rabbit secondary antibodies conjugated with Alexa 488, 568 or 647 were used as appropriate (Thermo Fisher Scientific). For fixed F-actin labelling, phalloidin pre-conjugated with Alexa 488, 568 or 647 was used as appropriate (Thermo Fisher Scientific). DAPI (4′,6-diamidino-2-phenylindole dihydrochloride; Thermo Fisher Scientific) nucleic acid stain was used as a nuclear marker as appropriate.

Immunofluorescence labelling was performed either manually or using liquid-handling robotics (Freedom EVO, Tecan) to minimize experimental variability, as described previously[59]. In either case, standardized procedures were used except where otherwise stated. Cells were fixed with 4% paraformaldehyde (PFA; Sigma-Aldrich) for 20 min, washed three times with phosphate-buffered saline (PBS) and permeabilized using 0.1% TX-100 (Sigma-Aldrich) for 5 min at room temperature. Cells were then blocked for 15 min with 1% BSA in PBS (PBS/BSA). Primary antibody immuno-labelling then proceeded at room temperature for 30 min. After PBS/BSA washing, secondary antibodies conjugated with either Alexa 488, 568 or 647 fluorophores were applied for 30 min at room temperature. Finally, cells were washed three times with PBS.

Immunoblotting was performed on SDS–polacrylamide gels with proteins transferred to Immobilon-P-Membranes (Millipore). Membranes were probed with anti-talin-2 mouse monoclonal (68E7; Abcam) at 1:500 dilution, anti-α-tubulin (DM1A; Thermo Fisher Scientific) at 1:500 dilution, or anti-integrin β5 (4708S; Cell Signalling Technology) at 1:1,000 dilution. Proteins were detected using enhanced chemiluminescence (ECL) reagent (Amersham Pharmacia Biotech).

Imaging. Live- and fixed-cell imaging was primarily performed using either a Nikon Ti2-mounted A1R confocal microscope running NIS elements software (Nikon) with a PlanApo VC ×60/1.4 numerical aperture (NA) oil-immersion objective or a Leica TCS SP5 acousto-optical beamsplitter confocal microscope using a ×63 objective (HCX Plan Apochromat, NA 1.25) and LCS software (Leica). Live fluorescence imaging during cell division was carried out with a Yokagoawa CSU-X1 spinning-disk confocal and Andor electron-multiplying charge-coupled device (EM-CCD). TIRF imaging employed a Nikon Ti2 inverted microscope configured for minimal (~90 nm) evanescence wave penetration. Live-cell imaging intervals were 0.5–5 min over 1–8 h with pixel resolutions between 0.13 and 0.21 μm. Live cells were maintained in normal culture medium, absent FCS/FBS (fetal calf serum/fetal bovine serum), at 37 °C and 5% CO_2. Live cell interference reflection microscopy (IRM) made use of a Zeiss LSM 510 confocal microscope and Plan-Apochromat ×63/1.4 NA oil objective, with post-sample dichroic mirror displacement allowing reflected laser light (561 nm) detection.

Fluorescence recovery after photobleaching (FRAP) analyses were performed via confocal microscopy and analysed as described previously[60]. Briefly, three sequential images were acquired of integrin β5-2GFP and mCherry-vinculin in U2OS-β5V cells before bleaching, enabling robust recovery standardization. Both reticular and focal adhesions (2–3 each per cell) were then bleached using 35% of maximal 488 nm laser power over 40 rapid iterations (<3 s per cell). Recovery was monitored for a total of 1,875 s, with intervals of 6 s for the first 120 s and intervals of 45 s thereafter.

STORM was performed in U2OS cells fixed during either interphase or mitosis. Cells were labelled using rabbit polyclonal anti-integrin β5 antibody (ab15459) and with Alexa 405–Alexa 647 double-labelled secondary. Secondary antibodies (Jackson ImmunoResearch) were labelled in house, as previously described[61]. A Nikon *N*-STORM system with Apo internal reflection fluorescence ×100/1.49 NA objective was used, with images acquired using an EM-CCD camera. Before STORM imaging, TIRF images of integrin β5 and mCherry-vinculin were acquired, enabling diffraction-limited definition of reticular and focal adhesions using the criteria detailed in the section 'Image analysis'. Thereafter, 647 nm laser light excited Alexa 647, with 405 nm light used for reactivation. Standard STORM imaging buffer was used, containing 100 mM Cysteamine MEA, 0.5 mg ml^{-1} glucose oxidase, 40 μg ml^{-1} catalase and 5% glucose (all Sigma-Aldrich).

Image analysis. Patch Morphology Analysis Dynamic software (Digital Cell Imaging Laboratories) was used for analysis of static (fixed) and dynamic (live) cell imaging data, except where otherwise specified. Analysis strategy and parameterization were as described previously[20,21,59,62]. Briefly, both cells and intracellular adhesion cohorts were segmented according to pixel intensity gradient analysis. A variety of morphological, pixel intensity and dynamic properties were then extracted for each cell and for each adhesion[21]. Relationships between each adhesion and its (parent) cell were maintained. Minimal adhesion size was set to 0.3 μm^2. For live cell data, adhesion tracking parameters included linear motion interpolation over a maximum of one missing time point, 3 μm maximum adhesion step size per time point and four time point minimum track lifetime. When quantifying differences between reticular and focal adhesions, we used the absence or presence (respectively) of canonical adhesome components as a defining indicator. Specifically, we applied a threshold such that segmented adhesions (delineated by integrin β5) were defined as reticular if they contained less than the mean of background fluorescence values (pixel intensities inside the cell boundary but outside segmented adhesions) plus two standard deviations for a canonical adhesion marker (vinculin or talin). Integrin β5-positive adhesions with greater than this value of fluorescence (for the canonical adhesion marker) were classed as focal adhesions.

For FRAP analyses, PAD software was used to segment integrin β5-2GFP-positive adhesions found in the last (third) pre-bleach image frame. Focal and reticular adhesions were distinguished based on mCherry-vinculin content, as described above. Identical adhesion boundaries (from pre-bleach frame 3) were then used as fluorescence recovery measurement locations for all subsequent image

frames. Adhesions judged to move during this period were excluded from further analysis. Integrin β5-2GFP fluorescence recovery curves were first standardized relative to intensity fluctuations (including non-specific photobleaching) in non-bleached areas of the cell. Thereafter, intensity values in bleached regions were standardized per adhesion as a percentage of the mean of the three pre-bleached images. The standard deviation of percentage recovery, per time point, was also recorded. Recovery curves are displayed as mean per time point (circles) ± 95% confidence intervals (CIs; per time point). Loess regression defined a smoothed fit (line) ± a moving 95% CI envelope. Statistical differences between Loess fitted curves were assessed via two-sided Kolmogorov–Smirnov testing.

STORM data were analysed using Insight3 software (developed by Bo Huang, University of California). Localization coordinates were first precisely defined via Gaussian fitting. Next, reticular and focal adhesions were segmented and defined using conventional TIRF images of integrin β5 and vinculin, based on the thresholding criteria detailed above. Clustering was then performed on integrin β5 localizations within each adhesion type, revealing coordinate position and localization counts for integrin nanoclusters found within each adhesion. DBSCAN was used for clustering[63], with epsilon (search radius) set to 10 nm and minimum points (within epsilon radius) set to 3. Nearest-neighbour distances between nanoclusters and localization numbers per cluster were assessed for each adhesion type using R.

Three-dimensional rendering and animation of confocal images was performed using NIS elements software. Additional supplementary movies were prepared in FiJi software[64].

MS analysis of the reticular adhesome. Four 10-cm-diameter dishes per condition of U2OS cells were cultured for 48 h to 90% confluency then treated with either DMSO or 20 μM cytochalasin D (Sigma-Aldrich) for 2 h. To isolate adhesion complexes, cells were incubated with the membrane-permeable crosslinker dimethyl-3,3′-dithiobispropionimidate (DTBP, Sigma-Aldrich; 6 mM, 5 min). DTBP was then quenched using 1 M Tris (pH 8.5, 2 min), after which cells were again washed once using PBS and incubated in PBS at 4 °C. Cell bodies were then removed by a combination of cell lysis in RIPA buffer (50 mM Tris-HCl, pH 8.0, 5 mM EDTA, 150 mM NaCl, 1% (wt/vol) TX-100, 1% (wt/vol) sodium deoxycholate (DOC), 0.5% (wt/vol) SDS; 3 min) and a high-pressure water wash (10 s). Protein complexes left bound to the tissue culture dish were washed twice using PBS, recovered by scraping in 200 μl recovery solution (125 mM Tris-HCl, pH 6.8, 1% (wt/vol) SDS, 15 mM dithiothreitol), and incubated at 70 °C for 10 min. Each sample was subsequently precipitated from solution by addition of four volumes of −20 °C acetone, incubated for 16 h at −80 °C, and resuspended in reducing sample buffer.

For MS, samples were separated by SDS–PAGE on a 4–12% SDS Bis-Tris gel (Thermo Fisher), stained for 10 min with Instant Blue (Expedeon), and washed in water overnight at 4 °C. Gel pieces were excised and processed by in-gel tryptic digestion as previously described[4]. Peptides were analysed by liquid chromatography (LC)–tandem MS (MS/MS) using an UltiMate 3000 Rapid Separation LC (RSLC, Dionex Corporation) coupled to an Orbitrap Elite mass spectrometer (Thermo Fisher). Peptides were separated on a bridged ethyl hybrid C18 analytical column (250 mm × 75 μm inner diameter, 1.7 μm particle size, Waters) over a 1 h gradient from 8 to 33% (vol/vol) ACN in 0.1% (vol/vol) FA. LC–MS/MS analyses were operated in data-dependent mode to automatically select peptides for fragmentation by collision-induced dissociation (CID). Quantification was performed using Progenesis LC–MS software (Progenesis QI, Nonlinear Dynamics; http://www.nonlinear.com/progenesis/qi-for-proteomics/). In brief, automatic alignment was used, and the resulting aggregate spectrum filtered to include +1, +2 and +3 charge states only. A .mgf file representing the aggregate spectrum was exported and searched using Mascot (one missed cleavage, fixed modification: carbamidomethyl [C]; variable modifications: oxidation [M]; peptide tolerance: ± 5 ppm; MS/MS tolerance: ±0.5 Da), and the resulting .xml file was re-imported to assign peptides to features. Three separate experiments were performed, and abundance values for proteins identified in the analysis were used to determine which proteins were enriched over twofold following treatment with cytochalasin D. Although 53 proteins were detected in the original MS data, four were excluded from further analysis due to their high representation in the CRAPome database[30]. The putative reticular adhesome interaction network was constructed using the online STRING protein–protein interaction database (v. 10)[65] including experimentally validated interactions only, with a 'medium' interaction confidence score (>0.4). Even at higher confidence (interaction confidence score > 0.7), this interaction network is dense: 91 known interactions relative to 11 randomly expected (based on proteome-wide interaction frequencies). Biological process- and KEGG pathway-enrichment analyses were performed using the DAVID Bioinformatics resource[66].

PIP regulator siRNA screening and drug-based perturbation of PtdIns(4,5)P_2 and Arp2/3. U2OS-β5V cells were treated with pooled siRNAs (four siRNAs per target; ON-TARGET SMART Pool plus; Dharmacon) via reverse transfection in the inner 60 wells of 96-well optical glass plates. Each plate contained five negative (untreated, mock transfected and three non-targeting siRNA controls) and three positive targeting controls (against EGFP, integrin αv or integrin β5). The primary screen was repeated twice, with a secondary validation assay using four siRNAs individually per target (Dharmacon) also repeated twice. siRNA sequences are presented in Supplementary Table 5. To prepare the siRNA library, 1 μl of each siRNA pool from 2 μM stock was mixed with 30 μl nuclease-free water and added to 96-well glass-bottomed-plate wells, before drying at room temperature. For reverse transfection, 30 μl of RNAiMAX was first added to 9 ml of Opti-MEM (Thermo Fisher Scientific). Then, 30 μl of this mixture was added to each well, followed by 30 min incubation. U2OS-β5V cells (90% confluent) grown in 75 cm^2 flasks were trypsinized and resuspended with 30 ml of growth medium. A 100 μl volume of the resulting cell suspension was added to each well and pipetted five times to disperse cells. The final siRNA concentration was 15 nM. Cells were incubated for 48 h before fixation with 4% PFA (15 min) and subsequent permeabilization with 0.2% TX-100 in PBS. Finally, cells were incubated for 1 h with DAPI and Alexa 647-conjugated phalloidin before PBS washing three times.

Cells were imaged with a Nikon A1R confocal microscope with a PlanApo VC 60X/1.4 NA oil-immersion objective. Image settings were identical for all samples and repeats. Montage images were acquired and stitched in NIS elements software, enabling high-resolution acquisition of ~100 cells and ~5,000 adhesions per condition per experimental repeat. Image data were quantified and analysed using KNIME software. Individual cells were segmented using Voronoi tessellation based on DAPI (nuclei) and phalloidin (cell body) staining. Integrin β5-positive adhesions were then segmented and split using spot detection and the Wählby method[67], respectively. Focal and reticular adhesions were defined based on mCherry-vinculin content as described above. Background-corrected intensity values were extracted per channel, for each adhesion, per cell. Mean integrin β5 intensity values in reticular adhesions were divided by values in focal adhesions to generate the relative intensity ratio. All values were *Z*-score standardized using robust statistics (median and median absolute deviation) relative to the combination of (three) non-targeting siRNA controls per 96-well plate. Resulting response distributions were plotted using R and RStudio software.

U2OS-β5V cells cultured and plated as described above, including 48 h incubation in 96-well optical glass plates, were treated for 30 min with DMSO (control), 10 mM neomycin (PtdIns(4,5)P_2 binding inhibition) or 25 μM LY294002 (inhibition of PtdIns(3,4,5)P_3 generation). For treatment with Arp2/3 inhibitor, U2OS cells plated onto glass coverslips and cultured for 48 h were treated for 2 h with 50 μM CK-666 (Arp2/3 inhibitor) or 50 μM CK-689 (Arp2/3 inhibitor control; inactive analogue of CK-666). Cells were then fixed, permeabilized and labelled as described above. Imaging and analysis were again performed using KNIME, as described above for siRNA screening.

Talin knockdown and response analysis. Talin-1-null mouse embryonic stem cells (mES talin $1^{-/-}$; gift from D. Critchley, University of Leicester) were transfected using RNAiMAX (Thermo Fisher Scientific) according to the manufacturer's instructions using either non-targeting control siRNA (ON-TARGETplus non-targeting control; 5′-UGGUUUACAUGUCGACUAA-3′) or talin-2-specific siRNAs designated talin-2 siRNA1 (5′-GCAGAAUGCUAUUAAGAAAUU-3′), talin-2 siRNA2 (5′-CCGCAAAGCUCUUGGCUGAUU-3′) or talin-2 siRNA3 (5′-AAGUCAGUAUUACGUUGUUUU-3′). siRNAs were synthesized by GenePharma. Cells were incubated for 48 h then plated for 3 h on 10 μg ml^{-1} vitronectin. Fixation and permeabilization conditions were tuned to retain cytoplasmic talin-2, as described previously[59]. Briefly, labelling was performed using liquid-handling robotics (Freedom EVO, Tecan) to reduce experimental variability. Cells were fixed with 2% PFA for 10 min, washed with PBS, and permeabilized using 0.1% TX-100 for 5 min at room temperature. Cells were then blocked for 15 min with 1% PBS/BSA. Immuno-labelling followed at room temperature for 30 min, targeting integrin β5 (polyclonal Ab; ab15459, Abcam) and talin (pan-talin mouse monoclonal Ab '53.8', BioRad) or anti-talin-2 mouse monoclonal Ab '68E7' (Abcam). After 1% PBS/BSA washing, Alexa 488 and 647 secondary antibodies were applied, targeting rabbit and mouse primary antibodies, respectively. Images of integrin β5 and residual talin-2 were acquired with a Nikon A1R confocal and oil-immersion objective (PlanApo VC ×60/1.4 NA). Image analysis was performed using PAD software to record residual talin (mean) intensities per cell, mean β5 intensities per segmented adhesion (per cell) and cell area. Values were scaled as fold-change relative to control siRNA. A total of 20–40 cells were imaged per condition in each of four experimental repeats with talin-2 siRNA1, or single confirmatory experiments with talin-2 siRNA2 and 3. Immunoblotting was performed as described above.

Integrin β5 knockdown and mitotic analysis. siRNA used for knockdown of β5 targeted the sequence 5′-GGGAUGAGGUGAUCACAUG-3′ and was obtained from Dharmacon. For rescue of β5 expression, an siRNA-resistant WT β5-EGFP clone was generated using the QuickChange IIXL site-directed mutagenesis kit (Agilent Technologies) to introduce silent mutations in the siRNA target sequence. The primers were forward 5′ -AGCCTATGCAGGGACGAAGTTATTACCTGGGTGGACACC-3′ and reverse 5′-GGTGTCCACCCAGGTAATAACTTCGTCCCTGCATAGGCT-3′ (obtained from Eurofins Genomics).

Cells were transfected simultaneously with either non-targeting or β5 siRNA together with either EGFP alone (pEGFP-N1 empty vector; gift of P. Caswell,

University of Manchester) or WT β5-GFP using Lipofectamine 2000 (Thermo Fisher) according to the manufacturer's instructions. Six hours after transfection, cell cycle synchronization was initiated by adding 2 mM thymidine (Sigma). After 18 h, cells were released by replating in fresh medium, and a second dose of thymidine was added 8 h later. Medium was replaced the next morning and imaging started 5 h after the second release.

Images were acquired on an ASMDW live-cell imaging system (Leica) equipped with a Cascade II EM-CCD camera (Photometrics) and a ×20/0.50 NA plan Fluotar air objective. Images were collected every 10 min using Image Pro 6.3 software (Media Cybernetics) and processed using ImageJ.

Mitotic alignment analysis. Before analysis of mitotic alignment, image files were computationally blinded by randomized file name encoding. Thereafter, Fiji software was used to measure the angular difference between the long axis of the mother cell before cell division, and the axis of cytokinesis. All observed cell division events were analysed. Where multiple attempts at cytokinesis were observed, the orientation of the first attempt was used for angular measurement. Data were summarized using R software.

Adhesion assay. Cell adhesion assays were performed as described previously[68]. Briefly, non-tissue culture-treated, polystyrene 48-well cluster plates (Corning Costar Corporation) were coated with 10 μg ml^{-1} vitronectin as detailed above, and blocked with 1% heat-denatured BSA. A total of 5×10^4 CS1-wt (negative control) or CS1-β5 cells were seeded per well and allowed to attach for 30 min under incubation conditions. Cells were treated during attachment as indicated with combinations of cytochalasin D (20 μM) and either cyclic RAD (Arg-Ala-Asp; non-inhibitory control) or cyclic RGD (competitive inhibitor of integrin β5-vitronectin interaction) peptides (20 μg ml^{-1}) (provided by Merck and used as described previously[69]). After attachment, non-adherent cells were removed by repeated washing. Remaining cells were labelled with DAPI and imaged with a Nikon A1R confocal microscope and ×10 air objective, enabling automated cell counting via NIS elements software.

Statistics and reproducibility. Except where otherwise stated, all data presented reflect at least three biologically independent experiments. For analyses based on per cell quantification and/or intracellular adhesion population analyses, exact cell and/or adhesion numbers are given in the figure legends.

Statistical analyses and graphical representation were predominantly performed using R software (v. 3.5.1) and RStudio (v. 1.1.453), or in some cases within Excel. All raw quantitative data and R analysis code are provided in the 'Code availability' section. Image analyses were predominantly automated via either commercial PAD software (v. 6.3) or open-source KNIME software (v. 3.6.0), ensuring uniform treatment and reproducibility. A representative KNIME image analyses workflow as well as sample images and subsequent data integration workflows are provided in the 'Code availability' section. Manual image analyses were performed in ImageJ following computational blinding of the image data identity. All graphical data representations are provided in the figure legends, as well as statistical significance testing and correction procedures. For data visualization, boxplot notches indicate ±1.58 times the interquartile range divided by the square root of the observation number, approximating the 95% CI. Except where otherwise stated, error bars also represent 95% CIs, estimated as described above. Statistical significance tests were all unpaired and two-tailed, and included either *t*-testing (for small, parametric data sets) or Mann–Whitney *U*-testing (for large, potentially non-parametric data sets). Holm–Bonferroni corrections were applied to correct for multiple hypothesis testing. *P* values are presented numerically in each instance.

Reporting Summary. Further information on research design is available in the Nature Research Reporting Summary linked to this article.

Code availability. Where associated with open-source software tailored for this study, code underpinning this study is available through an associated public GitHub repository (https://github.com/locusJ/Lock-et-al-NCB-2018-Reticular-Adhesions-Data-and-Analysis-Repository). This includes a custom KNIME image quantification workflow used in automated analysis of siRNA and drug perturbation screening, and an associated custom KNIME data integration workflow. Sample images from the analysis of Arp2/3 inhibition effects are also included. An R markdown script coding for the majority of graphical outputs and statistical significance testing is included, as is the associated HTML notebook summarizing this process and results. This R code calls the multi-sheet Excel file provided as Supplementary Table 1, which contains all presented quantitative data. In some cases, graphical analyses were generated directly in Excel; these are embedded within relevant sheets of this file.

A file titled 'Instructional Workflow for Data Exploration and Reproduction.pdf' is provided within this repository, and outlines the use of included code and data.

Data availability

MS data have been deposited at the ProteomeXchange Consortium via the PRIDE partner repository with primary accession codes PXD008645 and PXD008680. Source data for Fig. 4a–d and Supplementary Fig. 4a,b are provided as Supplementary Table 2. All other quantitative data are presented in Supplementary Table 1, while sample images from screening analyses are provided via the GitHub repository described under 'Code availability'. All additional data supporting the findings of this study are available from the corresponding authors on reasonable request.

References

57. Smilenov, L., Forsberg, E., Zeligman, I., Sparrman, M. & Johansson, S. Separation of fibronectin from a plasma gelatinase using immobilized metal affinity chromatography. *FEBS Lett.* **302**, 227–230 (1992).
58. Yatohgo, T., Izumi, M., Kashiwagi, H. & Hayashi, M. Novel purification of vitronectin from human plasma by heparin affinity chromatography. *Cell Struct. Funct.* **13**, 281–292 (1988).
59. Kiss, A. et al. Non-monotonic cellular responses to heterogeneity in talin protein expression-level. *Integr. Biol.* **7**, 1171–1185 (2015).
60. Li, Z. et al. Integrin-mediated cell attachment induces a PAK4-dependent feedback loop regulating cell adhesion through modified integrin αvβ5 clustering and turnover. *Mol. Biol. Cell.* **21**, 3317–3329 (2010).
61. Bates, M., Huang, B., Dempsey, G. T. & Zhuang, X. Multicolor super-resolution imaging with photo-switchable fluorescent probes. *Science* **317**, 1749–1753 (2007).
62. Shafqat-Abbasi, H. et al. An analysis toolbox to explore mesenchymal migration heterogeneity reveals adaptive switching between distinct modes. *eLife* **5**, e11384 (2016).
63. Ester, M., Kriegel, H.-P., Sander, J. & Xu, X. A density-based algorithm for discovering clusters in large spatial databases with noise. *Proceedings of 2nd International Conference on Knowledge Discovery and Data Mining* **KDD-96**, 226–231 (1996).
64. Schindelin, J. et al. Fiji: an open source platform for biological image analysis. *Nat. Methods* **9**, 676–682 (2012).
65. Szklarczyk, D. et al. STRING v10: protein–protein interaction networks, integrated over the tree of life. *Nucleic Acids Res.* **43**, D447–D452 (2015).
66. Huang, D. W., Sherman, B. T. & Lempicki, R. A. Systematic and integrative analysis of large gene lists using DAVID bioinformatics resources. *Nat. Protoc.* **4**, 44–57 (2009).
67. Wählby, C., Sintorn, I. M., Erlandsson, F., Borgefors, G. & Bengtsson, E. Combining intensity, edge and shape information for 2D and 3D segmentation of cell nuclei in tissue sections. *J. Microsc.* **215**, 67–76 (2004).
68. Yebra, M. et al. Requirement of receptor-bound urokinase-type plasminogen activator for integrin αvβ5-directed cell migration. *J. Biol. Chem.* **271**, 29393–29399 (1996).
69. Strömblad, S. et al. Loss of p53 compensates for αv-integrin function in retinal neovascularization. *J. Biol. Chem.* **277**, 13371–13374 (2002).

nature research

Corresponding author(s): Lock, Strömblad

Reporting Summary

Nature Research wishes to improve the reproducibility of the work that we publish. This form provides structure for consistency and transparency in reporting. For further information on Nature Research policies, see Authors & Referees and the Editorial Policy Checklist.

Statistical parameters

When statistical analyses are reported, confirm that the following items are present in the relevant location (e.g. figure legend, table legend, main text, or Methods section).

n/a	Confirmed	
☐	☒	The exact sample size (*n*) for each experimental group/condition, given as a discrete number and unit of measurement
☐	☒	An indication of whether measurements were taken from distinct samples or whether the same sample was measured repeatedly
☐	☒	The statistical test(s) used AND whether they are one- or two-sided *Only common tests should be described solely by name; describe more complex techniques in the Methods section.*
☐	☒	A description of all covariates tested
☐	☒	A description of any assumptions or corrections, such as tests of normality and adjustment for multiple comparisons
☐	☒	A full description of the statistics including central tendency (e.g. means) or other basic estimates (e.g. regression coefficient) AND variation (e.g. standard deviation) or associated estimates of uncertainty (e.g. confidence intervals)
☐	☒	For null hypothesis testing, the test statistic (e.g. *F*, *t*, *r*) with confidence intervals, effect sizes, degrees of freedom and *P* value noted *Give P values as exact values whenever suitable.*
☒	☐	For Bayesian analysis, information on the choice of priors and Markov chain Monte Carlo settings
☒	☐	For hierarchical and complex designs, identification of the appropriate level for tests and full reporting of outcomes
☐	☒	Estimates of effect sizes (e.g. Cohen's *d*, Pearson's *r*), indicating how they were calculated
☐	☒	Clearly defined error bars *State explicitly what error bars represent (e.g. SD, SE, CI)*

Our web collection on statistics for biologists may be useful.

Software and code

Policy information about availability of computer code

Data collection	NIS elements software (Nikon), LCS software (Leica) and LSM (Zeiss).
Data analysis	Patch Morphology Analysis Dynamic software (Digital Cell Imaging Laboratories, Belgium) was used for analysis of static (fixed) and dynamic (live) cell imaging data in most cases. FIJI was used for analysis of mitotic axis alignment. KNIME (v3.6.0) was used for analysis for siRNA- as well as PIP and Arp2/3 drug-responses. NIS elements was used for 3D / 4D image data rendering. R (v3.5.1) was used for statistical data analyses and visualisation via RStudio (v1.1.453), although some analyses and graphical outputs were generated directly within Excel. STORM data were analysed using Insight3 software. Mass spectrometry quantification was performed using Progenesis LC-MS software (Progenesis QI, Nonlinear Dynamics, Newcastle, UK). R code as well as Knime image analysis and data integration workflows are available via the GitHub repository: https://github.com/locusJ/Lock-et-al-NCB-2018-Reticular-Adhesions-Data-and-Analysis-Repository This repository also includes all quantitative source data (as presented in Supplementary Table 1) and sample image data from Arp2/3 drug inhibition studies (for use in Knime image analysis workflows). Instructions as to the content and use of this repository are included in an associated .pdf file "Instructional Workflow for Data Exploration and Reproduction.pdf".

For manuscripts utilizing custom algorithms or software that are central to the research but not yet described in published literature, software must be made available to editors/reviewers upon request. We strongly encourage code deposition in a community repository (e.g. GitHub). See the Nature Research guidelines for submitting code & software for further information.

Data

Policy information about availability of data

All manuscripts must include a data availability statement. This statement should provide the following information, where applicable:

- Accession codes, unique identifiers, or web links for publicly available datasets
- A list of figures that have associated raw data
- A description of any restrictions on data availability

The mass spectrometry proteomics data have been deposited to the ProteomeXchange Consortium via the PRIDE partner repository with the dataset identifiers PXD008645 and PXD008680.
Quantitative data underlying graphical figure panels are available via the GitHub repository: https://github.com/locusJ/Lock-et-al-NCB-2018-Reticular-Adhesions-Data-and-Analysis-Repository
in the file "Supplementary Table 1 Statistics Source Data.xlsx"
Figures with associated raw quantitative data include: 1A; 1H; 2A; 2B; 2C; 2D; 2N; 2S; 2T; 2V; 2W; 3C; 3D; 3E; 3H; 3I; 5B; 5C; 5D; 6A; 6B; 6M; 6N; 7E; 7F; 8A; 8B; 8C; Supp F5C; Supp F6A.
The GitHub repository also contains sample image data from Arp2/3 drug inhibition studies (for use in Knime image analysis workflows). Instructions as to the content and use of this repository are included in an associated .pdf file "Instructional Workflow for Data Exploration and Reproduction.pdf".

Field-specific reporting

Please select the best fit for your research. If you are not sure, read the appropriate sections before making your selection.

☒ Life sciences ☐ Behavioural & social sciences ☐ Ecological, evolutionary & environmental sciences

For a reference copy of the document with all sections, see nature.com/authors/policies/ReportingSummary-flat.pdf

Life sciences study design

All studies must disclose on these points even when the disclosure is negative.

Sample size	Reticular adhesions are previously uncharacterised, in terms of their morphology, dynamics, content and functional influence. Therefore, no prior knowledge existed to guide prediction of sample sizes that might optimally mediate comparisons between reticular and classical adhesion characteristics. For this reason, sample sizes were based on standards in the field (such as for FRAP analysis), or based on the number of cells / adhesions accessible through automated imaging and analysis (where sample number typically exceeds current gold standards). At no time were the results of statistical comparisons (e.g. Mann-Whitney U test) used to motivate additional experiments aiming to achieve statistical significance.
Data exclusions	As described in text, 4 proteins detected in raw mass spectrometry data were excluded due to over-representation in a database of common contaminant proteins (CRAPome database, Mellacheruvu et al., 2013).
Replication	All experiments were successfully replicated. The number of replicates is specified for each experiment.
Randomization	Sample randomization was not relevant to this study because analysed populations were assigned to classes based on objective measures of identity (e.g. reticular versus classical adhesions defined by consistent quantitative criteria).
Blinding	Analysis of mitotic division axis alignment was manual and therefore computationally blinded. All other analyses were automated and therefore non-blinded.

Reporting for specific materials, systems and methods

Materials & experimental systems

n/a	Involved in the study
☒	☐ Unique biological materials
☐	☒ Antibodies
☐	☒ Eukaryotic cell lines
☒	☐ Palaeontology
☒	☐ Animals and other organisms
☒	☐ Human research participants

Methods

n/a	Involved in the study
☒	☐ ChIP-seq
☒	☐ Flow cytometry
☒	☐ MRI-based neuroimaging

Antibodies

Antibodies used	Primary antibodies used are described in Supplementary Table 4. Anti-mouse and anti-rabbit secondary antibodies conjugated with Alexa 488, 568 or 647 were used as appropriate (Thermo Fisher Scientific). For fixed F-actin labelling, phalloidin pre-conjugated with Alexa 488, 568 or 647 was used as appropriate (Thermo Fisher Scientific). DAPI (4', 6-Diamidino-2-Phenylindole, Dihydrochloride; Thermo Fisher Scientific) nucleic acid stain was used as a nuclear marker as appropriate.
Validation	Details per Ab provided in Supplementary Table 4.

Eukaryotic cell lines

Policy information about cell lines

Cell line source(s)	All cell lines were acquired directly from either ATCC or ECACC, with the exception of H1299, CS-1 and talin 1 null mouse embryonic stem cells.
Authentication	Cell lines acquired directly from either ATCC or ECACC have been authenticated by the provider. H1299, CS-1 and talin 1 null mouse embryonic stem cells were not authenticated.
Mycoplasma contamination	All cell lines were tested and found to be negative for mycoplasma
Commonly misidentified lines (See ICLAC register)	No cell lines used in this study were found in the database of commonly misidentified cell lines (v8.0) that is maintained by ICLAC and NCBI Biosample